ALGORITHM THEORETICAL BASIS DOCUMENT

RETRIEVAL OF GEOPHYSICAL PARAMETERS FROM MEGHA-TROPIQUES

Space Applications Centre
Indian Space Research Organization
Ahmedabad – 380015

September 2012

GOVERNMENT OF INDIA

I*NDIAN SPACE RESEARCH ORGANISATION*
SPACE APPLICATIONS CENTRE
AHMEDABAD – 380 015

DOCUMENT CONTROL AND DATA SHEET

1	**Date**	September 25, 2012
2	**Title**	Algorithm Theoretical Basis Document: Retrieval of Geophysical Parameters from Megha-Tropiques
3	**Version**	3.0
4	**Document No.**	ISRO/SAC/MT-UP/Retrieval-03/ September-2012
5	**Type of Report**	Scientific
6	**No. of pages**	80
7	**Authors**	MT-UP Geophysical Parameter Retrieval Task Team
8	**Originating Unit**	Space Applications Centre, Ahmedabad
9	**Abstract**	This document describes the theoretical basis for the retrieval of various geophysical parameters from various sensors of Megha-Tropiques satellite.
10	**Classification**	General
11	**Circulation**	All concerned

Table of Contents

1.0 Introduction

1. Introduction

Megha-Tropiques (MT) a satellite realized under ISRO-CNES collaborative mission was launched on October 12, 2011 using ISRO's PSLV (Polar Satellite Launch Vehicle) in an inclined 20° orbit at an altitude of 867 km to understand the energy and water cycles in the global tropical region. The MT satellite frequently measures radiation emitted by the Earth-Atmosphere System in the visible, infrared and microwave spectrum through its four sensors onboard namely, MADRAS (Microwave Analysis and Detection of Rain and Atmospheric Structures), SAPHIR (Sondeur Atmosphérique du Profil d'Humidité Intertropical par Radiométrie), ScaRaB (Scanner for Radiation Budget) and ROSA (Radio Occultation Sensor for Atmosphere). The MADRAS system is a five-channel (18.7 GHz, 23.8 GHz, 36.5 GHz, 89 GHz and 157 GHz), dual polarized (except 23.8 GHz), self-calibrating, microwave radiometer system with azimuth scanning of ±65° yielding data swath of 1700 kms at local incidence angle of 53.5° at the Earth's surface. The SAPHIR sensor is a microwave humidity sounder operating around 183.31 GHz with six-channels (±0.2, ±1.1, ±2.8, ±4.2, ±6.8 and ±11 GHz) with cross-track scanning of ±43° yielding data swath of 1705 Km with variable local incidence angle at the Earth's surface. The ScaRaB sensor operates in four bands (0.55-0.65 μm, 0.2-4.0 μm, 0.2-50.0 μm and 10.5-12.5 μm) with a swath of 2242 km with cross-track scanning of ± 48.9°. ROSA tracks the dual-frequency L-band signals, transmitted by the GPS-GNSS, in both the fore and aft direction from limb sounding geometry giving 1-dimensional (vertical) profile of geophysical parameters at various geo-locations of the earth.

The major task is the retrieval of various geophysical parameters from MT sensors involving complexities of the inverse problem and the characteristics of the instruments. This draft document describes the theoretical basis of the algorithms for retrieving various geophysical parameters from these sensors. These algorithms are planned for the implementation on the operational basis for geophysical data product generation from MT satellite data. Algorithms for each sensor are provided in separate sections as presented in this document.

Section 2 describes the details of rainfall retrieval from MADRAS which includes the state of the art of algorithms for retrieving rainfall rate using microwave radiometers, scattering based radiative transfer model, necessity of environmental and hydrometeor data sets, inversion techniques, prevailing retrieval accuracies and validation techniques.

Section 3 deals with the retrieval of geophysical parameters namely, atmospheric total water vapour content, cloud liquid water content and ocean surface wind speed from MADRAS. It describes the global scenario including Indian heritage, emission based radiative transfer model, simulation of environmental data, simulation based retrieval techniques, fine-tuning and validation techniques.

Section 4 is devoted to the retrieval of atmospheric humidity profile from SAPHIR sensor. It deals with the emission based radiative transfer model suitable for sounding purpose, simulation of synthetic atmospheric profiles, sensitivity studies, simulation results, inversion techniques and preliminary analysis of limited AMSU-B sounder data.

Section 5 describes the complexities of processes needed for estimation of top-of-atmosphere radiation flux from the radiance measurements over the different portions of the electromagnetic spectrum by ScaRaB.

Section 6 deals with the retrieval of atmospheric profiles of temperature and humidity using the information about the refractivity as an input made available from ROSA measurements.

2.0 Retrieval of Rainfall from MADRAS

2. Retrieval of Rainfall from MADRAS

2.1 Algorithm configuration information

2.1.1 Algorithm name:
Rainfall Retrieval (RAINRET)

2.1.2 Algorithm Identifier:
ISRO_MT_RAINRET_A001

2.1.3 Algorithm Specification

Version	Prepared by	Description
2.0	R.M. Gairola and A.K. Varma	ATBD for Rainfall Retrieval from MADRAS

2.2 Introduction

Rainfall is a highly discontinuous process both in space and time. Accurate and reliable measurements of rainfall over extensive areas of oceans present a formidable challenge to meteorologists. In addition to large uncertainties in the derived estimates, there are problems related to nonuniformities of coverage, quality and logistics of operations etc. The global observations and monitoring of clouds from space using remote sensing techniques, has the potential of providing global rainfall information on desired time and space scales (Kummerow et al. 1995, Adler et al. 1994). Precipitation is associated with various atmospheric phenomena both in small and large scale. Assessment of precipitation contributes to improve weather forecasting, in small and large spatial scales, and a study of global rainfall leads to better understanding of global climate variability.

In addition, one of the strongest links between ocean, land and atmosphere is the fresh water fluxes due to evaporation and precipitation process. Evaporation ("E") controls the loss of fresh water and precipitation ("P") governs most of the gain of fresh water. Inputs from rivers and melting ice can also contribute to fresh water gains. Evaporation minus precipitation is usually referred to as the net flux of fresh water or the total fresh water in or out of the oceans and can be determined from satellite remotes sensing methods (Gairola et al. 2007). E-P determines surface salinity of the ocean, which helps determine the stability of the water column. Salinity and temperature determine the density of ocean water, and density influences the circulation. Precipitation also affects the height of the ocean surface indirectly via salinity and density. The global increase in oceanic evaporation (E) is determined by the increase in surface heating and this controls the global increase in precipitation (P). With the global warming scenario, it has been argued that increased moisture content of the atmosphere favours stronger rainfall events, thus increasing risk of flooding over land and more fresh water fluxes (E-P) over the oceans. It changes the buoyancy of the sea waters and also acts as a forcing function in OGCM.

The development of rainfall estimation techniques based on remote sensing measurements from space has registered tremendous progress and realistic achievements over the last three decades. Like any other fields of endeavor, however, there are limitations too and newer and better measurement and estimation techniques are developed on a continuous basis. The ability of space based measurements to provide a 2-D distribution of rainfall over large areas with sufficiently frequent sampling in time, especially over data sparse oceanic regions, facilitates us with a tremendously powerful tool to detect, closely monitor monsoon system and study the genesis and evolution of the furious tropical cyclonic storm.

Most tropical rainfall that has an impact over more than world's two-third population occurs as a result of convective processes. Understanding rainfall and its variability will contribute significantly to making reliable monsoon forecast. In addition, the knowledge of precipitation as one of the initial state of the atmosphere is necessary in weather prediction for physical initialization of numerical models. For years the need for diabetic initialization of precipitation in numerical models is being fulfilled by the infrared measurements by polar and geostationary satellites, since IR/VI measurements are continuously available with larger viewing areas and high resolution.

Microwaves can penetrate clouds and to some extent rain, and thus provide another source for rainfall estimation over both land and oceans. Over the years, passive microwave (PM) instruments on earth orbiting platforms have been providing valuable information for precipitation estimation. The applications that benefited from microwave rainfall estimates include weather forecasting, climate analysis, and hydrological studies. The successful use of PM-based rain estimates in applications from various fields encourages the continuation of efforts toward the development of more advanced rain retrieval algorithms, despite obvious limitations associated with the low sampling frequency of orbiting platforms carrying PM sensors. The recent availability of detailed precipitation observations jointly obtained by the first space-borne precipitation radar (PR) and a multifrequncy passive microwave radiometer, the TRMM Microwave Imager (TMI), on NASA-USA and NASDA-Japan's Tropical Rainfall Measuring Mission (TRMM) satellite offers an excellent opportunity for studying such issues. It can also supplement the observations from the IR/VIS measurements if properly integrated/unified and brings out the finer details than any one alone.

2.2.1 Overview and Background: Measurement of Rain by Space-Based Methods:

VIS/IR Measurements of Rain :

Digital image data from polar orbiting and geostationary meteorological satellites with synoptic coverage and quasi-continuous sampling in time have now become the major tools for attempts to monitor rainfall from space. The most common and easily exploited image data - cloud images in the visible and thermal IR bands - provide reasonably direct information on cloud areal extent, cloud type and cloud growth and decay. However, cloud formation to rainfall is an involved process. The Visible/IR sensing from space does not permit direct measurement of raindrops and hence provides essentially indirect inferences from which useful estimates of rain falling below the cloud may be derived.

Encouraged by the overpowering advantages of spacebased observations, even these proxy indicators have been exploited to severe as a basis for development of a variety of techniques for estimation of rainfall. The basic assumption that underlies all rainfall estimation techniques which utilize satellite images in the Visible and IR band is that raining clouds can be distinguished from non-raining ones : the former are usually thick and tall producing high visible band reflectance and cold cloud top temperatures. The possible physical basis for this lies mainly in the fact that cold high clouds represent signatures of upward motion in a locally saturated atmosphere indicating deep convection.

The available schemes use visible and/or IR imagery and time evolution of cloud characteristics e.g. merging of cumulus clouds, cloud bands, anvils etc. seen in hourly/half hourly images. Many of these schemes are interactive in nature.

Over the Indian region, monthly average rainfll information in the form of quantitative precipitation estimate (QPEs) maps with spatial resolution of 2.5^0x2.5^0 are produced on a regular basis since 1986 using INSAT-VHRR IR images collected eight times daily (Arkin et al. 1989). These maps are produced following the Arkin and Miesner (1987) tecnique. Currently rainfall estimation from IR and Water Vapour channels of KALPANA and INSAT-3A are being utilized for the development of advanced algorithms for rainfall estimation over land and oceanic regions at 2.5^0x2.5^0 and sub-grid scale (0.25^0x0.25^0) by Gairola et al. (2007) by both GPI and INSAT Multi Spectral Rainfall Algorithm (IMSRA) (Gairola et al. 2007).

Microwave Measurements of Rain:

Satellite microwave radiometers have been successfully used to monitor the temporal and spatial variations of sea surface and atmospheric properties on global scale since the launch of the Soviet Cosmos-243 instrument in 1969. The process of using satellite data for such applications is complex. Grody (1993) provided a complete review of past, present and planned future satellite microwave instruments, including their operational characteristics and applications. Among all the geophysical parameters, rainfall is the most difficult parameter to be retrieved from satellite remote sensing due to the intermittent nature of the processes of rain occurrence and its highly complex emission/absorption and scattering properties.

Microwave, due to their long wavelengths achieve better penetration and interact strongly with the raindrops present in the cloud. These measurements provide a direct physical basis for rain estimation. Also microwaves are largely intensive to the presence of ice in thin cirrus clouds but only suffers its poor resolution capability. The precipitation monitoring capability of SSM/I has been demonstrated by many investigators. Wilheit et al. (1991) used multichannel microwave measurements for the rainfall retrieval. Negri et al. (1989) discussed meteorological interpretations with the false color images of 85 GHz (HH, VV) and 37 GHz (VV) for precipitation processes and clarification of land, ocean and sea ice types with SSM/I. Berg (1992) estimated and analyze inter-annual variations in the tropical oceanic rainfall using data from SSM/I.).

Microwave radiances reaching satellite altitudes from precipitating clouds containing aspherical ice, combined phase hydrometeors and the background atmosphere (cloud liquid water, water vapor and gaseous constituents etc.) within the instrument field of view. The upwelling radiation observed by a microwave radiometer is expressed as an equivalent brightness temperature Tb and the ability

of passive microwave radiometer to infer rainfall depends largely on the contrast between the observed brightness temperatures over raining and non-raining areas. Some of the sensitivity studies have been carried out through radiative transfer simulation by (Swaminathan et al. 2005, Deiveegan et al. 2007, Viltard et al. 1998, Bauer et al. 1993, Gairola et al. 2001, 2005 etc) and through the empirical approach (Varma et al. 2003, Pokhrel et al. 2004 etc.) and showed the possibility of rainfall over Ocean and land regions.

Utilizing the frequency and polarization discrimination of passive microwave measurements from space, it has been successfully demonstrated that satisfactory rainfall retrievals both over land and oceanic areas are feasible. It has been seen that satellite estimates based on passive measurements portray the rainfall as accurately as radar both in terms of relative intensity and spatial distribution.

Rainfall over the oceans are retrieved relatively more reliably than over land. In total, the applications that benefited from microwave rainfall estimates include weather forecasting (Xiao et al. 2000), climate analysis (Hou et al. 2000), and hydrological studies (Petty and Krajwski 1996). The successful use of PM-based rain estimates in applications from various fields encourages the continuation of efforts towards the development of more advanced rain retrieval algorithms, despite obvious limitations associated with the low sampling frequency of orbiting platforms carrying PM sensors. The recent availability of detailed precipitation observations jointly obtained by the first space-borne precipitation radar (PR) and a multifrequency passive microwave radiometer, TMI, on NASA and NASDA's TRMM satellite (Simpsion et al. 1996) offers such an excellent opportunity for studying such issues.

Still with such missions dedicated to rainfall estimation, rain retrieval algorithms from PM radiometry suffer from various limitations. These limitations originate in the multiple hydrometeor profiles that can be associated with a set of multifrequency PM measurements (i.e., lack of unique solution The indeterminacy is more ever for overland retrievals because of the warm background brightness temperatures that limit the use of lower-frequency observations (i.e., 10, 19, and 22 GHz). Some algorithms, referred to as physically based, are derived using radiative transfer calculations through cloud-model simulated fields (Kummerow et al. 1996, Haferman et al. 1997). The physically based algorithms were mainly investigated in over ocean retrievals. Such physically based retrieval over land are few and have not indicated better performance relative to purely statistical algorithms (Druen and Heinemann 1998), which are conceptually simpler and more practical for applications.

In the beginning an algorithm for oceanic rainfall was developed for 19.35 GHz observations from Nimbus-5 Electrically Scanning Microwave Radiometer (ESMR) by Wilheit et al. (1977). Further modification to the algorithm was made by using statistical technique for multichannel data in the Nimbus-7 Scanning Multichannel Microwave Radiometer (SMMR) data (Wilheit and Chang 1980). Currently the 85 GHz channel in DMSP-SSM/I (F10, F11, F12, F13) and TRMM-TMI offers better possibilities of rainfall estimation. The optimal combination of integrated MW and IR observations offers a unique opportunity for rainfall retrieval more accurately (Gairola and Krishnamurti 1992, Gairola et al. 2005, Jobard and Desbois 1994, Adler et al. 1994, Liu et al. 1995). However it requires the rainfall from individual streams (either IR or MW based)

rain algorithms well placed. In addition to various SSM/I sensors presently available for the rainfall estimation, the Tropical Rainfall Measuring Mission (TRMM) provides the best opportunity with all type of passive (MW and VIS/IR) and active (MW) sensors onboard as a prelude to the Megha-Tropiques.

2.3. System Description

MADRAS (Microwave Analysis and Detection of Rain and Atmospheric Structures)

The proposed MADRAS system is a five-channel, self-calibrating, microwave radiometer system. This radiometer is designed to estimate atmospheric water parameters in the tropical belt. The choice of the channels has been driven by their potential contribution to the measurement of the parameters defined above, from the experience of processing other radiometer data. Table 1 below shows the brief description of MADRAS sensor.

Table 1: Channel of MADRAS and their related mission objectives

Channel No.	Frequency	Polarization	NEΔT	Spatial Resolution	Mission
M1	18.7 GHz	H+V	0.5 K	40km	Rain above oceans
M2	23.8 GHz	V	0.5 K	40km	Integrated water vapour
M3	36.5 GHz	H + V	0.5 K	40km	Liquid water in clouds, rain above sea
M4	89 GHz	H + V	1.0 K	10km	Convective rain areas over land and sea
M5	157 GHz	H + V	1.0 K	6km	Ice at cloud tops

2.4. Inputs

2.4.1 Static Data:

Parameter	Resolution	Accuracy	Source
Land/coast/sea flag	On the Footprints of each channel	--	DP
Global training dataset for temperature and humidity, RH, and hydrometeor profiles)	Surface to 50 hPa levels	--	TBD
Ground Truth, In-Situ Data	Point and pixel data of RG, MRR, AWS and DWR resp.		IMD, ISRO

2.4.2 Dynamic data:

Parameter	Resolution	Quantization	Accuracy	Source
Radiometric Brightness Temperature values of MADRAS channels #1-157 GHz	Each Pixel	TBD	--	Derived from raw data by DP
Geolocation information	each pixel		1 pixel	Derived by DP

2.4.3 Other Auxiliary data:

Sensor error estimates from sensor group.

2.5. Algorithm functional specifications

2.5.1 Overview:

Microwave brightness temperatures measured from a satellite-borne radiometer results from the integrated effects of surface emission and reflection, absorption and emission by atmospheric gases, and absorption, emission and multiple scattering of cloud and precipitation particles. Once scattering in the atmosphere becomes important (at 85.5 GHz, in particular for cases two and four), the influence of the model treatment of multiple scattering overrides the surface effect. To accurately describe the microwave signatures, a radiative transfer model with full inclusion of the aforementioned effects, particularly the multiple scattering by precipitation particles, is required.

The Theory of radiative transfer basically describes the interaction and propagation of radiative energy in a medium. As radiation is the most important source of energy for driving all the atmospheric processes and also atmospheric dynamics is strongly influenced by how solar and the terrestrial radiations are scattered, absorbed and emitted by the earth's surface and the atmosphere. Thus the knowledge of radiative transfer is most fundamental in the retrieval of atmospheric and earth's surface parameters in space-borne remote sensing. The extensive coverage of radiative transfer formulations has been made by Chandrasekhar (1960).

2.5.2 Theoretical Background:

It is the fundamental integro-differential equation, which governs the variation of intensity in a medium characterized by a spectral volumetric absorption coefficient, $K_v(s)$, and a spectral volumetric scattering coefficient, $\sigma_v(s)$, where s is the distance along the absorbing path.

Let us define the spectral volumetric extinction coefficient as

$$\beta_v(s) = K_v(s) + \sigma_v(s)$$

Finally dividing 3 equation by $\beta_v(s)$ we get

$$\frac{1}{\beta_v(s)} \frac{dI_v(s,\Omega)}{ds} + I_v(s,\Omega) = J_v(s,\Omega) \tag{1}$$

Where

$$J_\nu = \frac{j_\nu}{\beta_\nu(s)} = (1-\omega_\nu)B(T) + \frac{\omega_\nu}{4\pi}\int_{\Omega'} P(\cos\theta)I_\nu(s,\Omega')d\Omega' \qquad (2)$$

is referred to as the source function and

$$\omega_\nu = \frac{\sigma_\nu(s)}{\beta_\nu(s)} \qquad (3)$$

is called the single-scattering albedo, or particle albedo and expresses the fraction of the attenuated beam which is lost to scattering alone.

Equation 5 is the general equation of transfer and it is fundamental in the discussion of any radiative transfer process.

The RTE for Plane-Parallel Atmosphere

In plane-parallel atmospheres the medium is stratified in planes perpendicular to a given direction z, such that the optical properties of the medium are functions of z and ν only. Since thickness of a planetary atmosphere is generally small compared with its radius, thus this assumption is universally applied.

From figure we have $\dfrac{d(\ )}{ds} = \cos\theta\dfrac{d(\ )}{dz} = \mu\dfrac{d(\ )}{dz}$

Thus equation 3 in terms of z, μ, and φ :

$$\frac{\mu}{\beta_\nu(z)}\frac{dI_\nu(z,\mu,\varphi)}{dz} + I_\nu(z,\mu,\varphi) = J_\nu(z,\mu,\varphi) \qquad (4)$$

here in J_ν,

$$d\Omega' = \sin\theta'd\theta'd\varphi' = -d\mu'd\varphi' \qquad (5)$$

so that

$$J_\nu(z,\mu,\varphi) = (1-\omega_\nu)B_\nu[T(z)] - \frac{\omega_\nu}{4\pi}\int_0^{2\pi}\int_{-1}^1 P(\cos\theta_0)I_\nu(z,\mu',\varphi')d\mu'd\varphi' \qquad (6)$$

For convenience, introducing the concept of optical depth, τ_ν, measured from the outer boundary downward as

$$\tau_\nu = \int_z^\infty \beta_\nu(z')dz'$$

$$d\tau_\nu = -\beta_\nu(z)dz \qquad (7)$$

Thus replacing height variable z by optical depth τ_ν in equation (2.18) we have

$$-\mu\frac{dI_\nu(\tau_\nu,\mu,\varphi)}{d\tau_\nu} + I_\nu(\tau_\nu,\mu,\varphi) = J_\nu(\tau_\nu,\mu,\varphi)\,\text{or}$$

$$\mu\frac{dI_\nu(\tau_\nu,\mu,\varphi)}{d\tau_\nu} = I_\nu(\tau_\nu,\mu,\varphi) - J_\nu(\tau_\nu,\mu,\varphi) \qquad (8)$$

with

$$J_\nu(\tau_\nu,\mu,\varphi) = (1-\omega_\nu)B_\nu[T(\tau_\nu)] + \frac{\omega_\nu}{4\pi}\int_0^{2\pi}\int_{-1}^1 P(\cos\theta_0)I_\nu(\tau_\nu,\mu',\varphi')d\mu'd\varphi' \qquad (9)$$

Equation (8) is the basic equation for the problem of radiative transfer in the plane-parallel atmosphere, which is extremely difficult to solve. Part of difficulty is due to the azimuthal dependence of I_ν through the phase function. By expanding

the phase function in a Legendre polynomial series, the azimuthally dependent terms in the function can be uncoupled. Only the azimuthally independent equation contributes to the flux calculations, which is of greatest interest in most atmospheric applications. Thus confining our solution for the azimuthally independent equation.

Radiative transfer models:

The following two radiative transfer models are being used at SAC for simulations and sensitivity studies.

1. Eddington approximations

In Eddington approximation it is assumed that for an isotropic field the ratio of the second moment of the radiation field to the mean intensity is everywhere equal to 1/3.
In the plane parallel Eddington approximation, radiances are expanded in a series of Legendre and associated Legendre functions:

$$I_\nu(\tau_\nu, \theta, \varphi) = I_0(z) + I_1(z)\cos\theta + ... \qquad (10)$$

and the phase function is similarly expanded in Legendre polynomials

$$P(\cos\theta_0) = \sum_{l=0}^{N} \omega_l P_l(\cos\theta_0) = 1 + \omega_1 \cos\theta_0 + ... \qquad (11)$$

where θ_0 is the angle from θ', ϕ' to θ, ϕ, and the source function $J(z, \theta, \phi)$ can be written as

$$J_\nu(z, \theta, \varphi) = [1 - \omega(z)]T(z) + \omega(z)[I_0(z) + g(z)I_1(z)\cos\theta] \qquad (12)$$

where the asymmetry factor is given by $g = \dfrac{\omega_1}{3}$. Using this expression the isotropic component of the diffuse radiance I_0 can be deduced following (Weinman and Davies, 1978)

2. Discrete Ordinate Approximations

The radiative transfer equation 15 in terms of polarization p (H or V) can be expressed as (Tsang and Kong, 1977):

$$\mu \frac{d}{d\tau}\begin{bmatrix} I_V(\tau,\mu) \\ I_H(\tau,\mu) \end{bmatrix} = \begin{bmatrix} I_V(\tau,\mu) \\ I_H(\tau,\mu) \end{bmatrix} - \frac{\omega_0}{2} \int_{-1}^{1} \begin{bmatrix} P_{VV} & P_{VH} \\ P_{HV} & P_{HH} \end{bmatrix} \begin{bmatrix} I_V(\tau,\mu) \\ I_H(\tau,\mu) \end{bmatrix} d\mu' - (1-\omega_0)B(\tau)\begin{bmatrix} 1 \\ 1 \end{bmatrix}$$

(13)

Where all the symbols have their usual meaning. Here Plank function $B(\tau)$ is assumed to be linearly varying function of τ from the top of the layer (B_0) to the bottom of the layer i.e., $B(\tau)=B_0+B_1\tau$. The four scattering phase functions $(P_{VV}, P_{VH}, P_{HV}$ and $P_{HH})$ are the ones integrated over all azimuthal directions. Thus there exists cross-polarization scattering in the scattering source term because P_{VH} and P_{HV} are not zero. The exact solution of $Ip(\tau,\mu)$ is obtained by solving equation using the discrete ordinate method with sufficient streams. In this DOM model it is assumed that cross-polarization scattering in the scattering source term is negligible and the scattering phase function is assumed to follow Henyey-Greenstein equation, and is expended with Legendre polynomial (p_l) as

$$P(\cos\theta_0) = \frac{1-g^2}{(1+g^2-2g\cos\theta_0)^{\frac{3}{2}}} = \sum_{\ell=0}^{N}(2\ell+1)g^{\ell}p_{\ell}(\cos\theta_0) \equiv \sum_{\ell=0}^{N}A_{\ell}p_{\ell}(\cos\theta_0) \quad (14)$$

For azimuth-independent case (spheres, randomly-oriented irregular particles), the cosine of the scattering angle $\cos\theta_0$ can be denoted as $\mu\mu'$ (Liou, 1974), so that

$$P(\cos\theta_0) = P(\mu,\mu') = \sum_{\ell=0}^{N}(2\ell+1)g^{\ell}p_{\ell}(\mu)p_{\ell}(\mu') \equiv \sum_{\ell=0}^{N}A_{\ell}p_{\ell}(\mu)p_{\ell}(\mu') \quad (15)$$

Where asymmetry factor g is calculated following Mie theory (Bohren and Huffman, 1983), $p_{\ell}(\mu)$ is the lth order Legendre polynomial and N is the number of terms to add. In DOM, N=2n-1 (2n is the stream number). To minimize the error associated with this cutoff, a δ-adjustment (scaling g, τ, and ω_0) is applied following (Fu and Liou, 1992).

In performing numerical calculations, we divide the atmosphere into many layers and assume that all microphysical properties (e.g., particle concentration, liquid/ice water content, etc.) are uniform within each layer, but temperature varies linearly with optical depth. By solving the L_js the radiances at quadrature angles (μ_i) are obtained. A boundary condition at the surface allows us to calculate the upward radiation at surface given the surface emissivity and temperature. Using this analogy of calculating downward radiation from top layer to surface, upward radiance can be can continuously calculated from the bottom of the layer to the top of the layer and letting τ = 0 until the radiance at the top of the layer is solved. The satellite observed radiance at the top of the atmosphere is then obtained. Brightness temperature can be calculated from the radiance using Plank's function. Horizontally and Vertically polarized radiances are calculated separately because of the difference of their surface emissivity.
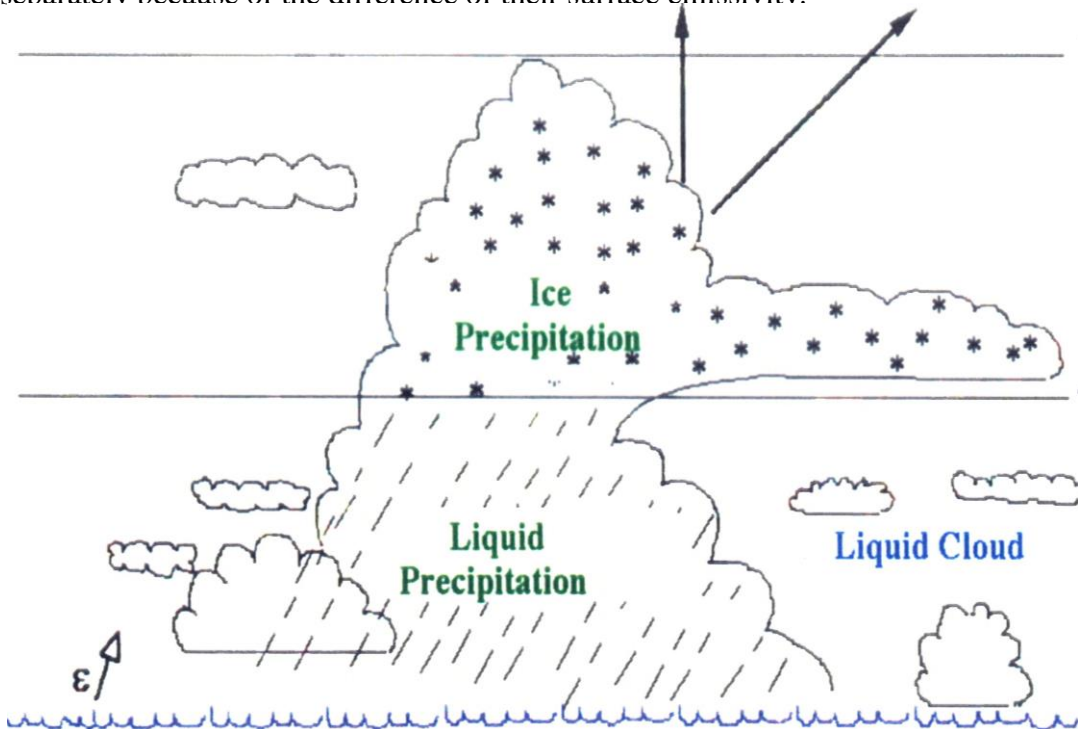

Fig. 1 Schematic Diagram Showing a Passive Microwave Signal for Rain Detection

Some results of the simulation and sensitivity studies are carried out for different frequencies (6.6, 10, 18, 21, 37 and 85 GHz), for various weather conditions that include raining and non-raining atmosphere and different sea states. Three components of the troposphere are important absorbers. Water vapor, liquid water and molecular Oxygen. Frequencies where absorption due to molecular Oxygen is important (roughly 50 to 70 GHz and near 119 GHz) are used for temperature sounding but are not often used for rainfall sensing. For our purposes, the absorption due to molecular Oxygen is a minor correction needed to be quantitatively correct but not necessary for conceptual understanding.

2.5.3 Algorithm Description:
Based on the above brief presentation of the formulation of both emission and scattering based radiative transfer, it is highly desirable to create a data based of input and output field vectors for the algorithm development to estimate rainfall using the MADRAS frequency channels. However the algorithm is required to be derived from radiative transfer calculations through an atmospheric cloud model (Tripoli et al.1992, Tao et al. 1993) specifying vertical distributions of ice, graupels, and other liquid hydrometeors as a function of rain rate. Such data base from cloud resolving models is very rare and is being explored. In liu of this, the algorithm is structured in two main classes. 1. Physically based: based on simulated data base as an advanced R & D and 2. Empirically based, based on the collocated matched data sets of MADRAS and Ground/Ocean truth data from various sources. Fig. 1 shows the schematic diagram of the rain detection from a passive microwave sensor. The Flow diagram is given in Fig. 2 (2.1 and 2.2) respectively. The complete algorithm steps are mentioned below:

1. Sensitivity studies through simulations of brightness temperatures for MADRAS frequency channels. Till the cloud microphysical data base is obtained, the artificially created data base along with ECMWF data will be used for radiative transfer simulations following (Liu et al.1998).

2. To ascertain the sensitivity of different channels to rainfall and other ocean and atmospheric variables, to decouple their influence for using in a rain-rate calculations in particular based on the above data base.

3. The screening process to distinguish between different land types, raining-nonraining background conditions associated with the emission and scattering characteristics of hydrometeors etc. using multichannel brightness temperatures from MADRAS (Following Ferraro et al. 1996 for SSM/I).

4. A matched data base of radiometer brightness temperatures and ground/ocaen rainfall from various sources (TRMM-PR, DWR, AWS, RG etc.) would be created. Based on the radiative transfer simulations as a bench mark, sensitivity studies and screening criterion mentioned above, would be applied to the data.

5. Following the background conditions and emission and scattering associated with hydrometeors, separate algorithms for land and oceans

will be developed based on the Scattering Index (SI) Method (by Ferraro et al. 1996).

6. Finally the rain rates will be retrieved using SI along with the collocated ground/ocean based data following multiple regression and/or Neural Network approach.

7. The resulting rain-rate estimates will be compared to four Doppler Weather Radars (DWR) as well as to buoys and shipboard measurements over a first 6-month period (during calibration/validation phase).

8. The retrieval algorithm would be attempted for the complete global estimates from the MADRAS based on the ground truth data availability from various continental and oceanic buoy and ship based sources.

9. The algorithm will be tested for its accuracy to describe both localized instantaneous rainfall events and global rainfall patterns over both land and oceans.
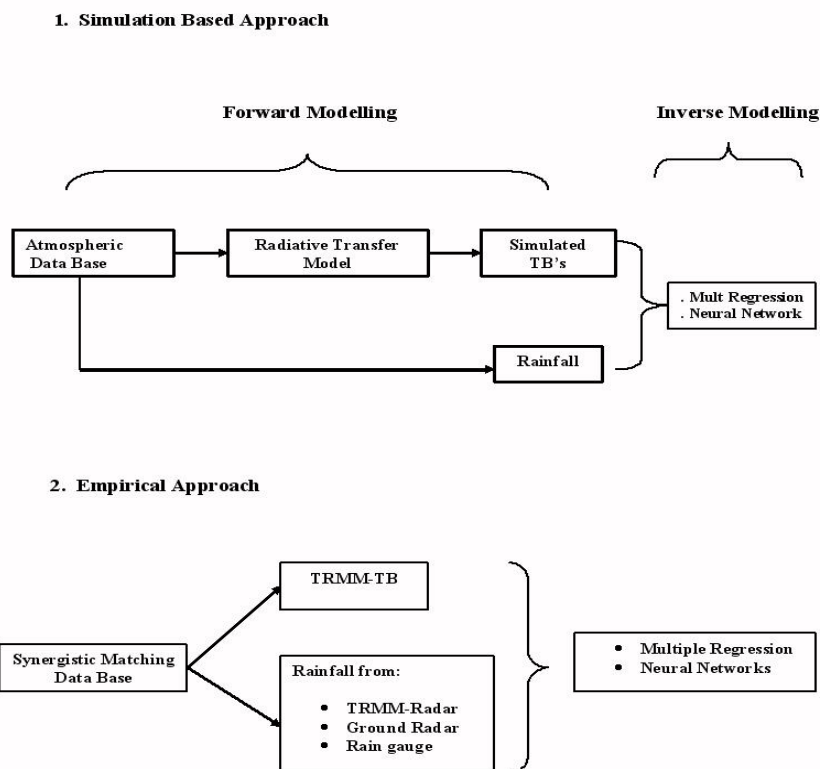

Fig. 2 Flow Diagrams showing the Concept of Rainfall Retrieval:

2.5.4 The inverse problem:

In the last decade, there has been a growing interest in developing rain profile retrieval algorithms trained by cloud radiative databases (Smith et al.1994). This

approach is based upon the use of radiative transfer models applied to cloud-resolving hydrometeor profile outputs. The appeal to develop fast inversion algorithms using pre-generated physically consistent cloud radiative databases has been largely exploited for spaceborne microwave radiometry of rainfall (Mugnai 1988 et al. and Kummero et al. 1996). Following this approach, the accuracy of rainfall estimates are basically linked to the accuracy of both forward and inverse models. In particular, the reliability and consistency of the various radiative transfer models, used for building retrieval databases, is a crucial problem to be investigated within this framework. As indicated, the simulations will be carried out as a reference bench mark for the proper selection of channels and their combinations. The real data base would be the collocated matched data base of TBs and ground based rainfall measurements.

Regarding empirical approach, a matched data sets of the MADRAS radiometric observations will be attempted in conjunction with the ground based observations from rain gauges, Doppler Weather Radars (DWR) etc. There are a couple of empirical approaches that could be attempted for the retrievals. These are simple multiple regressions between the rainfall and the brightness temperatures from MADRAS channels. Other methods are based on the SI, PCT and D approaches mentioned above section which are highly applicable for the rainfall retrievals. In order to demonstrate the applicability of empirical approaches, the existing data of TRMM radar and radiometric observations will be utilized and compared with the standard TRMM products of rainfall. The Fig. 3 shows the Logical Flow of Algorithm Development and Validation diagram to be used conceptually.
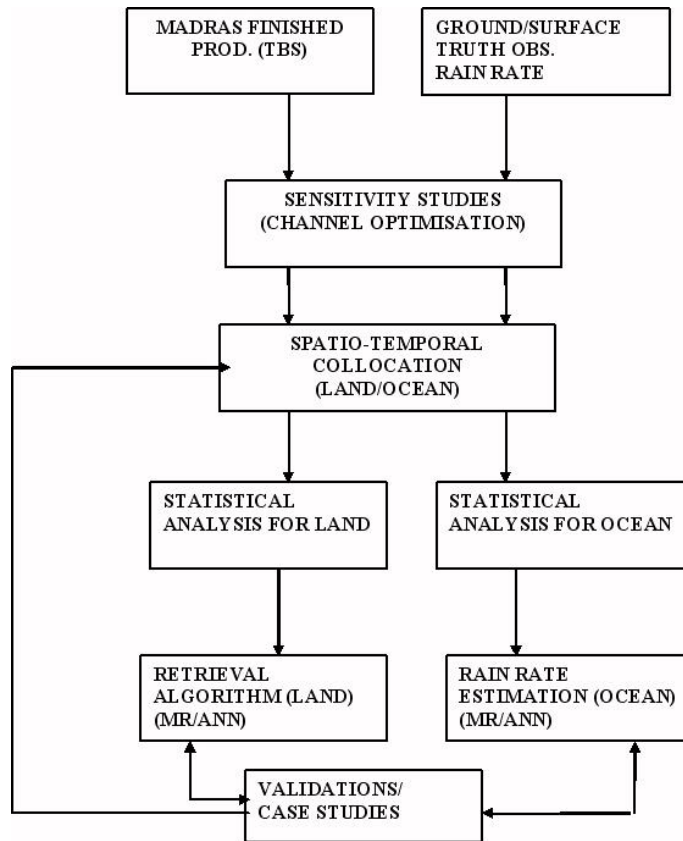
Fig. 3 Logical Flow of Algorithm Development and Validation

2.5.5 Instantaneous Ocean Rainfall

As is shown earlier that DOM based Radiative transfer calculations represents better simulations to determine a brightness temperature, Tb, given a temperature, water vapor and hydrometeor profile. An inversion procedure, however, is needed to find a rainfall rate, R, given a brightness temperature Tb. The double valued nature of the relations is encountered in 19 to 37 GHz channels as is shown in sensitivity section; however it could be resolved by a combination of two or more channels. Since Tbs are sensitive to the vertical structure of precipitation, the vertical structure cannot be ignored when instantaneous retrievals are sought. The sensitivity to the assumed profile gets larger as the frequency increases and the scattering in the upper layers of the cloud begin to play a larger role. The objective of the instantaneous rainfall algorithm over ocean is to be achieved using one of the suitable retrieval techniques, such as ANN, MR or Bayesian approach.

Predefined cloud structures, however, may be utilized to overcome the uncertainties in the accuracies of the retrievals. Cloud resolving models such as the Goddard Cumulus Ensemble model (GCE), which is a cloud microphysical model developed mainly by Tao and Simpson, (1993), or the Tripoli, (1992), model are used to supply the required cloud structures. For each cloud model time step, radiative transfer computations are supposed to be performed at high resolution.

Databases are generated separately for different freezing heights to capture the different
dynamics of tropical rainfall systems. Once a database of profiles and associated brightness temperatures is established, the retrieval employs a straightforward inversion methodology. In the absence of a suitable cloud model data base this approach will be taken up as a R & D effort.

Meanwhile, for an alternate operational algorithm development, an equally workable approach of the detection of rain over ocean would be employed. following For this purpose the data base of TRMM-TMI, and SSM/I radiometric TBs will be collocated with TRMM-Precipitation Radar over the global oceans. This data base will be used to develop a robust set of relationships with the SSM/I sensor (since the frequency channels and footprints of SSM/I are similar to MADRAS compared to TRMM-TMI). A matched data base of SSM/I-TBs and buoy and ship based rainfall would also be created based on the observations all over the tropical oceanic regions.

Further refinement of the technique is described in Ferraro *et al.* (1994) and Ferraro *et al.* (1998). The rationale was to first develop a relationship which could best predict the 85 GHz *Tb* under "nonscattering" conditions for the ocean surface in question. Then, by estimating this value and subtracting the actual 85 GHz *Tb*, a measure of the depression due to scattering by precipitation ice/rain drops could be determined.

The form of the Scattering Index method (*SI)* is as follows:

With the seven channels of SSM/I, we name $E(19V, 21V)_{85v}$ as the estimated value of TB_{85v} by TB_{19v} and TB_{21v}. Based on the data set of rain free areas, we will regress a formula $E(19v, 21V)_{85v}$ as follows, which was used to estimate the value of TB_{85v}:

$$E(19V, 21V)_{85v} = a + bTB_{19v} + cTB_{21v} + TB_{21v}^2$$

It has been well established (Yao et al. 2001, Mishra et al. 2007) that when it is not raining, $E(19V, 21V)_{85v}$ can represent well the value of TB_{85v}. The Scatering Index over the ocean thus can be defined as the difference between $E(19V, 21V)_{85v}$ (the estimated value of TB_{85v}) and TB_{85v} (the observed value of TB_{85v}):

$$SI_O = E(19V, 21V)_{85v} - TB_{85v}$$

$$SI_O = a + bTb_{19v} + cTb_{21v} + d\ Tb21^2_{22v} - Tb_{85v}$$

where the coefficients *a,b,c,* and *d* were derived by assembling a global data set of SSM/I observations under scatter-free conditions. Through an exhaustive evaluation, it could be found that a threshold *SI* value could be a good, global indicator of rain. A lower threshold does detect more rain; however, it also causes the detection of false alarms to increase. Because snow and deserts can cause a similar scattering signature, a set of "screens" would be developed to remove such features based on the screening approach of Ferraro et al. 1996. . The desert check involves the use of polarization information at 19 GHz, while the separation of rain from snow utilizes two relationships involving the *Tb* at 22 and 85 GHz.

Specifically, the following type of relationship would be attempted based on PR rain rate and SSM/I based SI_O to work best for tropical Indian Ocean and global oceanic regions.

$$RR \ mm/hr \ . = a \ SI_O{}^b$$

This method to retrieve rain rate would be compared with the standard products of rainfall from SSM/I and TRMM. TRMM provides various data sets on rain rates over both land and oceans in the form of surface rain rate, total rain in 3 hourly etc. Similarly SSM/I provides oceanic rain rates on instantaneous and accumulation on daily basis.

2.5.6. Instantaneous Land Rainfall

Over land, rainfall retrievals are far more complex and difficult than oceanic retrievals due to the large and variable emissivity of the land surface. Specifically, the high emissivity masks the emission signature that is related directly to the water content in the atmosphere. Instead, only the brightness temperature depression due to scattering in the upper portion of clouds is observed. The scattering, as shown in Figure 3, increases with increasing frequencies. Consequently, brightness temperature depressions at the 89 GHz channel of MADRAS will contain the least ambiguous signal of scattering by ice and/or large raindrops. The brightness temperature depression will be converted to an expected rainfall rate through the retrieval scheme where databases of hydrometeor profiles (associated with a variety of rain systems) will be developed for different climatological zones. Recent results from TRMM indicate that the relationship of lightning flashes (which is highly correlated with the 85 GHz scattering signature) and rainfall varies over the global land regions. Development of profile databases for different climatological zones can account for regional differences. However, as a starting point, we will insure that these retrievals match closely with established algorithms developed for the SSM/I and TMI sensors.

A further complication that arises over land is the lack of consistent backgrounds against
which to compare the *Tb* depression. To alleviate this problem caused by the varying emissivity associated with changes in surface characteristics (e.g., surface wetness, snow
cover, vegetation, etc.), a rain/no-rain temperature depression threshold is required. The "screening" issue has always been one of modest controversy in the land-based retrievals because of the empirical nature of their form. Intuitively, one immediately thinks that such screens will vary greatly with sensor. However, as is described later, these screens (i.e., *Tb* relationships separating rainfall from other surfaces) seem to hold valid for other sensors, with only minor modifications needed. Additionally, one school of thought in physical retrievals is that the rain rate retrieval becomes a two-step process: rain identification and rain rate determination.
The basis for the retrieval over land comes from the work of Grody (1991), who developed a global scattering index (*SI*) at 85 GHz for use with the SSM/I sensor. Further refinement of the technique is described in Ferraro *et al.* (1994) and Ferraro *et al.* (1998). The rationale was to first develop a relationship which could

best predict the 85 GHz *Tb* under "nonscattering" conditions for the land surface in question. Then, by estimating this value and subtracting the actual 85 GHz *Tb*, a measure of the depression due to scattering by precipitation ice/rain drops could be determined. The form of the *SI* is as follows:

$$SI_{85v} = a + bTb_{19v} + cTb_{21v} + d\ Tb21^2_{22v} - Tb_{85v}$$

 where the coefficients *a,b,c,* and *d* were derived by assembling a global data set of SSM/I observations under scatter-free conditions. Through an exhaustive evaluation, Grody (1991) found that an *SI* value of 10 K or greater was a good, global indicator of rain. A lower threshold does detect more rain; however, it also causes the detection of false alarms to increase. Because snow and deserts can cause a similar scattering signature, a set of "screens" were developed to remove such features. The desert check involves the use of polarization information at 19 GHz, while the separation of rain from snow utilizes two relationships involving the *Tb* at 22 and 85 GHz.

Ferraro *et al.*, (1994), built upon the Grody (1991) study, and developed a more robust set

of relationships to be used for the detection of rain over land from the SSM/I. In this study, separate relationships were developed for land and ocean, improving the sensitivity to scattering. In addition, the original relationships derived by Grody (1991) used antenna temperatures which were convolved to the 19 GHz *FOV*; the updated study used the more conventional *Tb* values and preserved the original SSM/I footprint sizes, allowing for easy implementation by the scientific community. An alternative method to retrieve rain rate has been to calibrate the *SI* with ground-based radar measurements from the United States, Japan, and the United Kingdom (Ferraro and Marks, 1995). Similar to the oceans, the following relationship would be attempted to work best for global oceans:

$$RR\ mm/hr\ . = a\ SIL^\beta$$

where *RR* is in mm/hr. Since these relationships increase rapidly for higher values of *SIL*,

any retrieval above 35 mm/hr is set to 35 mm/hr. Although somewhat arbitrary, practice

shows that this is the upward limit of rain rates retrievable from the 85 GHz measurements (e.g., the maximum mean rain rate that could exist in a 13 by 15 km *FOV*). Using the 10K minimum threshold for the *SIL* values, the minimum retrievable rain rate is approximately 0.5 mm/hr. This algorithm was implemented by FNMOC in 1995 as the operational SSM/I rain rate algorithm, and continues to operate in that capacity. In addition, the monthly derived rainfall from this algorithm (Ferraro, 1997) is used as a component of the GPCP blended analysis (Huffman *et al.*, 1996). The MADRAS instrument will contain nearly similar frequencies to the SSM/I. Initially the SSM/I based coefficients will be used and later fine tuned for MADRAS, based on a large data base to be co-located during raining episodes.

2.6. Operational Implementation: At MOSDAC

2.7. Outputs: Rainfall along the sub satellite tracks.

2.7.1 Format of the output and the domain: TBD

2.8 Validation

Extensive validation campaign is required during the first six months of the satellite launch. To compare retrieved rainfall totals with rainfall totals obtained by other satellites like TRMM and SSM/I will be attempted. Some more direct means, often called "Ground Truth", may also be attempted based on the aviaility of well calibrated data from AWS and DWR's. The initial six months will be the calibration-validation phase with limited distribution of data. The validation is possible with:

1. Other satellite data sets from regional and global sources (land & ocean).
2. Rainfall data from well calibrated DWR data from Indian Meteorological Department

The traditional approach has been to take a 2 dimensional rain field derived from radar measurements, assume it is constant in the third dimension and use the resultant pseudo 3 dimensional rain field for the simulation. This initial averaging step reduces the variability of the rain field and thereby reduces both the value and uncertainty of the BFC.

2.8.1 Data Required

Parameter	Resolution	Source
Doppler Weather Radar	0.25^0 x 0.25^0	From IMD at all DWR locations (every 1-3 hours)
Fast Response Rain Gauge	Usual point measurements over land & oceans	All daily obs. sites of IMD & to plan for oceanic locations
Micro Rain Radars	Point Measurements	
MADRAS/ TRMM /SSM/I Data	Orbital & analyzed data	Through Internet

2.8.2 Methods of Validation

The level 1a and level 1b products are required for above-mentioned approaches for the rainfall retrievals. The database created in an offline process will act as a tool for the algorithm development. During the initial six months of calibration-validation phase the knowledge of the noise characteristics of the different horizontal and vertical polarization channels will be applied for the improvement of the algorithm. This period will also help in creating a database of ground-based networks like rain gages, Automatic Weather Stations and Doppler Weather Radars in consistency with the MADRAS observations for the empirical algorithm development. The satellite overpasses in and around DWR and rain gauge sites will be utilized for the validation purposes. One complete iteration of TRMM rainfall validation campaign was exercised using the SHAR and IMD DWR at Chennai (Gairola et al. 2004) in a compaign mode. TRMM radar and radiometric observations of rainfall were compared with DWR on various grid scales. This needs to be augmented during the Megha-Tropiques time frame using all the five DWRs in the country, AWS and the fast response rain gauges. The error statistics will be generated with a possible feedback mechanism to correct for some biases etc. to make the algorithm more robust.

2.9 Technical Issues

For the instantaneous rainfall error there are some major sources of error:

1) Availability of Cloud resolving model simulations
2) Coastal boundaries.
3) Beam Filling Error
4) Vertical distribution of Hydrometeors
5) The freezing level retrieval

These error sources are very critical and needs to be followed with active groups working at various places elsewhere (in country or abroad).

2.10 Future Scope:

In the present document the possibilities of both physical and empirical algorithms for rainfall retrieval are highlighted. However due to certain limitations the empirical algorithm has been emphasized as an operational one. It would be based on the radiatiatve transfer simulations as the pointers to optimize the frequency channels. This is also important in view of the different noise scenario of the different channels to be known only after the launch of the satellite. Based on the performance of the algorithm over global tropical ocean and land, the fine tuning will be carried out. The ongoing advanced research on radiative transfer based algorithm will be worked out in future to generate the data base for retrievals. However, in any case an algorithm would be in place for its global applicability at par with the algorithms elsewhere for different satellite sensors like TRMM, SSM/I and GPM.

2.11 Reference

1. Adler, R. F., G.J. Huffman and P.R., Keehn, 1994., "Global tropical rain estimates from microwave adjusted geosynchronous IR data", Remote Sensing Rev. 11, 125-152.

2. Bauer, P. and P. Schluessel, 1993, "Rainfall, total water, ice water, and water vapor over sea from polarized microwave simulations and special sensor microwave/imager data", J. Geophys. Res., Vol 98, pp. 20,737.

3. Berg, W. and R. Chase, 1992: Determination of mean rainfall from the Special Sensor Microwave/Imager (SSM/I) using a mixed lognormal distribution, *J. Atm. Oceanic Tech.*, **9**, 129-141.

4. Chandrasekhar (1960). *Radiative Transfer*. Dover Publications, Inc.. ISBN 0-486-60590-6.

5. Deiveegan M, C. Balaji, and S. P. Venkatesha, Comparison of Various Methods for simultaneous Retrieval of Surface Emissivities and Gas Properties in Gray Participating Media

6. Druen, B. and G. Heinemann, 1998, "Rain rate estimation from synergetic use of SSM/I, AVHRR and meso-scale numerical model data", Meteor. Atmos. Phys., 66, 65-85.

7. Ferraro, R.R. and G.F. Marks, 1995, "The development of SSM/I rain-rate retrieval algorithms using ground-based radar measurements", J. Atmos. Oceanic Technol., Vol 12, pp. 755.

8. Ferraro RR, F. Weng, NC Grody and A. Basist, An eight year (1986-1994) time series of rainfall, clouds, water vapour, snow cover and sea ice derived from SSM/I measurements, Bulletin American Met. Soc. 77, 5, 1996.

9. Ferraro RR, NC Grody and GF Marks, Effects of surface conditions on rain identification using the DMSP-SSM/I, Rem. Sens. Rev. 1994, 11, 195-209.

10. Gairola RM, C Mallet, N. Viltard and E Moreau, 2001, "Rainfall from TRMM-TMI, 2nd ISRO-CNES Science Workshop on MEGHA-TROPIQUES", Paris, France, 1-5 July.

11. Gairola R.M., A.K. Varma, B.S. Gohil and V.K. Agarwal, "Sensitivity of radiative transfer to the oceanic surface roughness and rainfall for TRMM radiometric channels over Indian Oceanic regions", IJRSP 2005.

12. Gairola R.M., Samir Pokhrel, A.K. Varma, and V.K. Agarwal, A combine passive-active microwave retrievals of quantitative rainfall for TOPEX altimeter and TOPEX microwave radiometer, , *Int. Jour. Remote Sensing*, Vol. 20, April, 2005.

13. Gairola R.M. and T.N. Krishnamurti, 1992, "Rain rates based on SSM/I, OLR and Rain gauge data sets", Meteor. and Atmospheric Physics. 50, 165-174.

14. Gairola R.M., Anoop Mishra and A.K. Varma, Rainfall estimation from INSAT/KALPANA IR data using GPI approach and initial validations using AWS-data OSD/MOG/INSAT-3D/PR/SAC-2007

15. Gairola R.M., Samir Pokhrel, A.K. Varma, Vijay K. Agarwal and M.S. Narayanan,G. Viswanathan, Sanjay Sharma, Digant Sharma, Validation of TRMM Radar and Radiometric bservations of Rainfall using SHAR Doppler Weather Radar, Feb. 2004.

16. Gairola R.M. et. Al. (2007) Rainfall estimation from INSAT Multispectral Rainfall Algorithm (IMSRA) method, MOG Report. (under preparation).

17. Gairola R.M., Anoop Mishra, A.K. Varma, and V.K. Agarwal, Rainfall estimation using satellite MW and IR measurements over Indian land and oceanic regions, Submitted to Geophysical Research Letters, Sept. 2007.

18. Gairola R.M. and A.K. Varma, S. Pokhrel, V.K. Agarwal, Integrated satellite microwave and infrared measurements of precipitation during a Bay of Bengal cyclone, Ind. Jour. Radio & Space Physics, 33, 115-124, 2004.

19. Gairola, R.M., Samir Pokhrel[*], A.K. Varma, Abhijit Sarkar and Vijay K. Agrwal, Evaporation and Precipitation Estimates from TRMM Microwave Measurements, International Conference on Monsoon, IISc, Bangalore, 2007.

20. Haferman, J.L., E.N. Anagnostou, D. Tsintikidis, W.F. Krajewski, T.F. Smith, 1996: Physically Based Satellite Retrieval of Precipitation Using a 3D Passive Microwave Radiative Transfer Model. *Journal of Atmospheric and Oceanic Technology*: Vol. 13, No. 4, pp. 832–850.

21. Hou, Arthur Y., Sara Q. Zhang, Arlindo M. da Silva, William S. Olson, 2000: Improving Assimilated Global Datasets Using TMI Rainfall and Columnar Moisture Observations. *Journal of Climate*: Vol. 13, No. 23, pp. 4180–4195.

22. HuffmanG.J., R.F. Adler, P.A. Arkin, A. Chang, R. Ferraro, A. Gruber, J.J. Janowiak, R.J. Joyce, A. McNab, B. Rudolf, U. Schneider, and P. Xie, 1997: The Global Precip. Climatology Project (GPCP) Combined Precipitation Data Set. Bull. Amer. Meteor. Soc., 78, 5-20.

23. Jobard I. And M. Desbois, 1994, "Satellite estimation of the tropical precipitation using METEOSAT and SSM/I data", Atm. Res. 34, 285-298.

24. Kummerow C.W., and L. Giglio, 1995, A method for cmbining passive microwave and infrared rainfall observations J. Atmos. Ocean. Technol., 12, 33-45.

25. Kummerow C., 1993, "On the accuracy of Eddington approximation for radiative transfer in the microwave frequencies", Jour. Geophy. Res. 98, D2, 2757-2765.

26. Kummerow, C. D. W. S. Olson, and L. Giglio, "A simplified scheme for obtaining precipitation and vertical hydrometeor profiles from passive microwave sensors," *IEEE Trans. Geosci. Remote Sensing*, vol. 34, pp. 1213–1232, Sept. 1996.

27. Liu, G, 1998, A fast and accurate model for microwave radiance calculation, J. Meteor. Soc. Japan, 76, 335-343.

28. Liu G., J.A. Curry and R.S. Sheu, Classification of clouds over western equatorial Pacific Ocean using combined infrared and microwave satellite data, JGR, 100, 13,811-13,826, 1995.

29. Liu, G. and J.A. Curry, 1998, "An investigation of the relationship between emission and scattering signals in SSM/I data", Jour. Atmos. Sci., 1628-1643.

30. Mugnai A. and E. A. Smith, "Radiative transfer to space through a precipitating cloud at multiple microwave frequencies. Part I: Model description," *J. Appl. Meteor.*, vol. 27, pp. 1055–1073, 1988.

31. Negri, Andrew J., Robert F. Adler, Christian D. Kummerow, 1989: False-Color Display of Special Sensor Microwave/Imager (SSM/I) Data. *Bulletin of the American Meteorological Society*: Vol. 70, No. 2, pp. 146–151.

32. Petty, G.W., and W. Krajewski, 1996: Satellite rainfall estimation over land. *Hydrolog. Sci. Journ.,* **41**, 433-451.

33. Pokhrel S., AK Varma, RM Gairola, VK Agarwal, Distribution and intraseasonal variability of rain over Indian Oceanic region from Indian Remote Sensing Satellite IRS-P4 Multifrequency Scanning Microwave RadiometerJour. Geoph. Res., 108, C10, 3314, doi:10.1029/2003JC001886, 2003.

34. Simpson, J., C. Kummerow, W.K. Tao, and R.F. Adler, 1996: On the Tropical Rainfall Measuring Mission (TRMM). Meteorology and Atmospheric Physics: Vol. 60, pp. 19-36.

35. Smith E. A., C. D. Kummerow, and A. Mugnai, "The emergence of inversion-type profile algorithms for estimation of precipitation from satellite passive microwave measurements," *Remote Sens. Rev.*, vol. 11, pp. 211–242, 1994.

36. Spencer R.W., H.M. Goodman, and R.E. Hood, Precipitation retrieval over land and ocean with the SSM/I: identification and characteristics of the scattering signal. *J. Atmos. Oceanic Tech.*, **6**, 254-273, 1989.

37. Swaminathan V., R. M. Gairola, C. Balaji, S P Venkateshan, Estimation of microwave radiation intensity from a multi-layered cloud model,"AIAA Journal of Thermophysics and Heat Transfer *,19, 3, July-Sept, 2005.*

38. Tao, W. K. and Simpson J., 1993, "Goddard Cumulus Ensemble Model. Part I: Model Description", *Terr. Atmos. Oceanic Sci.*, **4**, 35-72

39. Tripoli, G.J., 1992, "An explicit 3-D non-hydrostatic numerical simulation of a tropical cyclone", *Meteor. Atmos. Phys.*, 49, 229-254.

40. Tsang L. and J. A. Kong, "Radiative transfer theory for active remote sensing of half-space random media," Radio Science, 13(5), 763-773, September-October 1978.

41. Varma, A.K., R.M. Gairola., A.K. Mathur, S. Pokrel, B.S. Gohil, and Agarwal, V.K., 2002, "Rain rate measurements over global oceans from IRS-P4 MSMR", Proceedings of Indian Academy of Sciences – Earth and Planetary Sciences 111, 257-266.

42. Varma, A. K., G. Liu, and Y.-J. Noh, 2004: Sub-pixel scale variability of rainfall and its application to mitigate the beam-filling problem. J. Geophys. Res. 109, D18210, doi:10.1029/2004JD004968.

43. Viltard, N., E. Obligis, V. Marecal and C. Klapisz, 1998, "Retrieval of precipitation from microwave airborne sensors during TOGA COARE", J. Appl. Meteor., 37, 701-717.

44. Weinman JA, Davies R. Thermal microwave radiances from horizontally finite clouds of hydrometeors. J Geophys. Res **1978**;83(6):3099–107.

45. Wilheit, TT, A.T.C. Chang, M.S.V. Rao, E.B. Rodgers and J.S. Theon, 1977, "A satellite technique for quantitatively mapping rainfall rates over the oceans", *J. Appl. Meteor.* 16, 551-560.

46. Wilheit, TT,, ATC Chang, and LS Chiu, Retrieval of monthly rainfall from microwave radiometric measurement using probability distribution functions, J.Atm. Ocean. Tech. 8, 118-136, 1991.

47. Wilheit, T. T., and A. T. C. Chang, 1980: An algorithm for retrieval of ocean's surface and atmospheric parameters from the observations of the Scanning Multichannel Microwave Radiometer. *Radio Science,* **15***, 525-544.

3.0 Retrieval of Geophysical Parameters over oceans from MADRAS

3. Retrieval of Ocean Surface Geophysical Parameters over oceans from MADRAS

3.1 Algorithm configuration information

3.1.1 Algorithm Name:
Retrieval of Ocean Surface Geophysical Parameters over oceans from MADRAS

3.1.2 Algorithm Identifier:
ISRO_MT_GPRET_A001

3.1.3 Algorithm Specifications:

Version	Prepared by	Description
3.0	Atul K. Varma, R.M. Gairola and B.S. Gohil	Other Parameters from MT

3.2 Introduction:

With the advent of well-calibrated satellite microwave radiometers, it is now possible to obtain long time series of geophysical parameters that are important for studying various atmospheric and oceanic processes. In order to strengthen the observation base to provide impetus to the studies concerning tropical processes, India and France have jointly proposed the Megha-Tropiques (MT) mission. In addition to a radiation budget instrument (SCAnner for RAdiative Budget: SCRAB), an atmospheric sounding instrument (SAPHIR), and a GPS receiver for occultation based profile measurements, the MT mission will also be carrying a microwave radiometer that designed specifically to measure rainfall and cloud/sea ice, and also the cloud liquid water, wind speed and water vapor over the global oceans. This radiometer is referred as MADRAS (Measurement and Detection of rain and Atmospheric Systems).

Microwave remote sensing program in ISRO started with the launch of its first microwave radiometer SAMIR-I onboard Bhaskara-I satellite in 1979 followed by similar payload SAMIR-II launched onboard Bhaskara-2 satellite in 1981. After a gap of nearly two decades, India launched microwave radiometer MSMR onboard Oceansat-1 (IRS-P4) satellite in May 1999. The MSMR provided the measured the measurements of radiances at 6.6, 10, 19 and 22 GHz channels. Gohil (1999) and Gohil et al. (2000a, 2000b) provided the description of the retrieval

algorithms for geophysical parameters like integrated water vapor (IWV), cloud liquid water (CLW), wind speed (WS) and sea surface temperature (SST) from the MSMR. Apart from these parameters MSMR was also exploited for rain measurements (Varma et al., 2002a, Varma et al., 2003, Pokhrel et al., 2003, Gairola et al, 2004)) even in the severe weather conditions like cyclone (Varma et al., 2006). The MSMR derived geophysical parameters were found to be in good agreement with ground and the other satellite observations (Varma et al., 2002b).

3.3 Overview and Background

This Algorithm Theoretical Basis Document (ATBD) focuses on the MADRAS microwave radiometer that is scheduled to fly in 2008/2009 on the MT mission. MADRAS will measure the Earth's radiation over the spectral range from 19 to 157 GHz. over the entire globe within tropics. The channel details and expected accuracies are given in the Table 1 (Desbois, 1999). For convenience, we will refer 18.7, 23.8, 36.5, 89 and 157 GHz frequencies as 19, 24, 37, 89 and 157 GHz, respectively. It will be possible to retrieve the three important geophysical parameters, IWV, WS and CLW. Rainfall can also be retrieved, which is discussed in a separate MT ATBD. The parameters are to be retrieved under the non-raining situations because at the microwave frequencies used for retrieval of the above parameters the emission due to rain is very strong and than obscure the effect of the other parameters. The table-2 provides the radiative transfer model calculated change in the brightness temperatures at 19, 21 and 37 GHz frequencies due to 1 mm h^{-1} of rain rate. It may be noted that a low raining condition of rain rate 1 mm h^{-1}, can even change the brightness temperature significantly.

Table: 1: Megha-tropiques sensor characteristics

Frequency	Polarization	Pixel size	NEDT sensitivity at 300 K
18.7	V & H	~ 50 km	0.5 K
23.8	V (or H)	~ 40 km	0.5 K
36.5	V & H	~ 25 km	0.5 K
89	V & H	~ 10 km	1 K
157	V & H	~ 6 km	1 K

Table 2: Brightness temperature for non-raining and low raining atmosphere.

For, SST =300 K, WS = 5 mm s^{-1}, CLW = 20 mg cm^{-2}			
	For Rain Rate = 0 mm h^{-1}	For Rain Rate = 1 mm h^{-1}	difference
Tb19 GHz V	216.16 K	228.57 K	12.41 K
Tb19 GHz H	160.06 K	182.40 K	22.34 K
21 GHz V	242.15 K	251.18 K	9.03 K
37 GHz V	236.27 K	257.16 K	20.89 K
37 GHz H	188.40 K	234.07 K	45.67 K

The sensitivity of the geophysical parameters to observing frequency is studied by Wilheit and Chang (1980). The study indicates high sensitivity for SST only at frequencies < 10 GHz. Hence the SST retrieval from MADRAS is not included in this document. The wind has high senstivity at 19 and 37 GHz channels but these channels are also affected by water vapor and cloud liquid water in the atmosphere. Gohil et al. (2000a) have shown that inclusion of lower frequency channels (6 GHz) in the wind retrieval algorithm improves the accuracy. This is mainly due to less influence of the water vapor and cloud liquid water on the lower frequency channels. Due to the absence of 10 and 6 GHz channels on MADRAS, wind retrieval accuracy will be slightly poorer compared to MSMR or TMI. The rms accuracies given in Table 3 come from SSM/I experience. We are hopeful that the retrieval accuracies for IWV, WS, and CLW will be almost similar to that available from SSM/I due to nearly identical lower frequency channels which are used for retrieval of the parameters being discussed in this document. However, *the radiometer noise is crucial to achieve this accuracy.*

Table -3: RMS error budget for retrieved parameters from SSM/I (Wentz, 1997)

Retrieval`	Atmospheric Model	Wind Direction	Radiometer Noise	Sampling Mismatch	Other	Total Observed
IWV	0.81	0.21	0.43	3.68	0.74	3.87

(m/s)						
WS (mm)	0.51	0.35	0.53	0.94	0.41	1.31
CLW (mm)	0.019	0.004	0.007	0	0.014	0.025

3.4 Objectives:

- Development of Algorithms for the retrieval of Integrated Water Vapor, Cloud Liquid Water and Wind Speed over oceans from Mega-Tropiques MADRAS.

3.5 Inputs

3.5.1 Static Data

We need following datasets for the retrieval of GPs. The datasets must represent global variability of the parameters.

- Temperature profiles
- Pressure Profiles
- Relative Humidity profiles
- Sea Surface Temperature
- Surface Wind Speed

We use the NCEP GFS reanalyzed model fields at 61 vertical levels with 500 m separation as input database for the RT model.

3.5.2 Dynamic Data

Following geolocated datasets are required.

Table -4

Parameter	Resolution	Quantization	Accuracy	Source
Tb 19 GHz V	Standard swath data with same grid (cell) size for all Tbs	0.01°	Standard dataset with predefined/proposed accuracy	DP
Tb 19 GHz H				
Tb 37 GHz V				
Tb 37 GHz H				
Tb 24GHz V				

3.5.3: Other auxiliary data

- Sensor error estimates from sensor group.

3.6. Algorithm Functional Specifications:

3.6.1: Theoretical background

Radiative Transfer Model

The brightness temperature received by microwave radiometer looking towards earth in non-scattering atmosphere in a thermodynamic equilibrium is given by:

$$Tb_v(\theta,p) = Tb_{DN} \, \tau(\theta) \, (1-\varepsilon(Ts, \theta,p)) + Ts \, \varepsilon(Ts, \theta,p) \, \tau(\theta) + Tb_{UP}$$

Where, Tb_v = brightness temperature measured at frequency v

Tb_{DN} = downwelling radiances

Tb_{UP} = upwelling radiances

v = frequency of observation

θ = angle of incidence

τ = transmittance

ε = emissivity
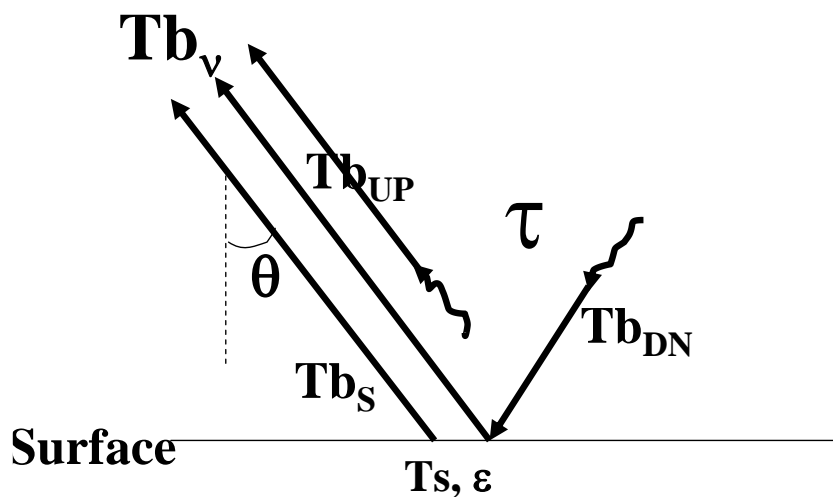
Ts = surface temperature

p = polarization

Fig. 1

The total brightness temperature has three components as mentioned in expression above and also in Fig. 1. First, the emitted radiation by the atmosphere directly reaching to the radiometer which mainly depends upon the absorption by atmospheric constituents like dominantly absorbing gases (oxygen and water

vapor) and the hydrometeors (water drops of cloud and rain). Second, the atmospheric radiation reaching the earth surface and gets reflected by it and reaches to the radiometer after having attenuated by the intervening atmosphere. Third, the radiation emitted by the earth surface after attenuated by the intervening atmosphere reaches to the radiometer. Thus, the total radiation received by the radiometer is affected by both atmosphere and earth surface.

We propose to use the standard stat-of-art radiative transfer models from Florida State University (Liu, 1998). In Liu's model the absorption models by Rosenkranz (1998) for oxygen and Rosenkranz (1993) for water vapour are used. Absorption due to non precipitating cloud is calculated using the model given by (Paris, 1971). The clouds will be simulated as given in the next paragraph. Liu's model (1992) utilizes Guillon et al. (1998) for calculating the ocean surface emissivity. The brightness temperatures thus simulated from the known atmospheric and surface geophysical variables are used to establish suitable statistical or physiostatistical relationships between them and atmpsheric parameters for retrieval purpose.

Masking the rainy area

A radiative transfer based method for rain identification over global oceans is developed prior the launch of the Megha-Tropiques satellite to avoid the retrieval of other GPs over oceans. The scheme is based on developing step-by-step procedures for transforming MADRAS based scattering index (SI) to equivalent SSM/I based scattering index with high accuracy (Varma et al., 2011).

Ferraro and Mark (1995) and Ferraro et al. (1996) provided a rain identification and retrieval algorithm over land and oceans. Their algorithm is based on empirical relationship between rain rate and scattering index which is originally proposed by Grody (1991). The Ferraro and Mark (1995) algorithm is developed for SSM/I channels and is not directly portable to MADRAS which is having different sensor characteristics. According to Grody (1991), scattering index (SI) is defined as depression in the SSM/I 85 GHz V polarized Tb (Tb85V) due to scattering in the presence of rain. They calculated the depression by taking the difference between observed rain-affected Tb85V and its expected value (Fs)

under rain free conditions. The expected Tb85V (Fs) under rain free conditions is worked out by establishing a relationship between SSM/I Tbs at 85.5 GHz V and at 19.35 GHz V & H and 22.23 GHz V channels that are essentially emission channels and are considered not to be affected by scattering. The relationship that they proposed for scattering index (SI) is as follows:

$SI = Fs - TbiV$,

where, TbiV is Tb from high frequency 85.5 GHz V polarized SSM/I channel, and F_s is expected TbiV under rain free conditions. The Fs is defined as,

$Fs = a_1*Tb1 + a_2*Tb2 + a_3*Tb3 + a_0$

These coefficients for SSM/I and MADRAS are calculated using radiative transfer simulated database of brightness temperatures under raining and non-raining conditions. This is shown schematically in Fig. 2 below.
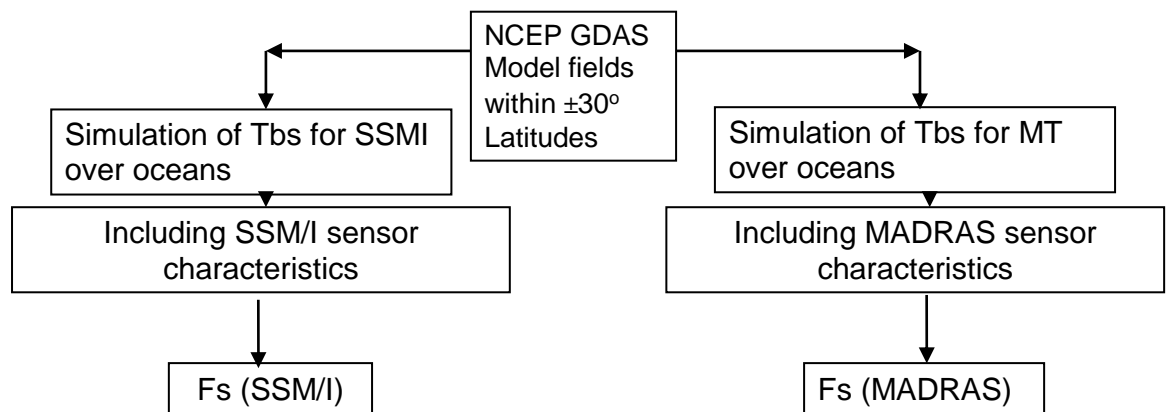

Fig. 2: Scheme for simulation of brightness temperatures for SSM/I and MADRAS using NCEP environment fields and finding regression relation for expected brightness temperature at 85.5 GHz (SSM/I) / 89 GHz (MADRAS).

In the next step a regression based relationship is established between SI (SSM/I) and SI (MADRAS). This relationship is used to estimate expected SI (SSM/I) for given SI (MADRAS). According to Ferraro and Mark (1995) and Ferraro et al. (1996), rain is expected when SI > 10. We use the same value of SI for identifying rain event.

Cloud Liquid Water Masking:

The high amount of CLW affects less to TPW retrieval but more to WS retrieval for WS being a surface parameter (Wentz, 1997). We therefore restrict the CLW value for the retrieval of the TPW and WS to 50 mg cm^{-2} and 18 mg cm^{-2}, respectively (Wentz, 1997). Thus if CLW exceeds these thresholds values, the TPW and WS are not retrieved.

Inversion Techniques:

Inversion techniques that are proposed to be employed have their heritage from MSMR, are essentially statistical techniques in which relationships between the predictors and the predictants are established. A general inversion technique is mathematically represented by the following expression:

$$G = D * \phi(Tb)$$

Here, G is a vector whose elements are various geophysical parameters which is related to a measurement basis function vector φ(Tb) of simulated brightness temperatures Tb by a matrix D. The measurement basis function vector contains the elements which could either be pure or functions of TB. The matrix D is given by:

$$D = C(\theta, \phi) \bullet C^{-1}(\theta, \phi)$$

where C is a correlation matrix and is obtained from geophysical variables' statistics.

Separate inversion coefficients are established for each geophysical variable. Different combinations of channels and polarization are required for different variable as the dependence of brightness temperature on these variables is different. Sensitivity studies and effect of errors in measurements on retrieval is also required for finalization of suitable combinations.

Effect of Sensor-Satellite System errors on retrievals:

As seen above that the retrieval coefficient matrix D is dependent on geophysical parameters as well as on the corresponding simulated brightness temperatures, the matrix D is affected by chosen statistics of geophysical parameters and on various errors in the brightness temperatures typical of a particular radiometer system and satellite attitude. It is always better for a stable retrieval to include the wide statistics of geophysical parameters and to account for various errors in the measurements of brightness temperatures by a radiometer and satellite attitude.

The dominant errors in the brightness temperature measurements are the system noise at antenna and radiometer system, calibration, uncertainties in knowing the actual measurement geometry (viz. incidence angle and polarization etc). Thus knowledge of total error in measurements is must for establishing the retrieval matrix which enables to provide better estimates of geophysical parameters with known errors as far as possible. The point to be noted here is that the retrieval will have errors in geophysical estimates from the erroneous data; however, the errors will be still more if we underestimate the overall error in brightness temperature and use such retrieval matrix D with actual data having even higher errors. On the other hand, the errors will also be more in parameters retrieved with matrix D established using overestimated errors and using it with less erroneous data. Therefore, it is must to know the true behavior of radiometer, system in terms of total error in brightness temperatures and the biases in the measurements. The next step is to fine-tune the retrieval matrix using the insitu data widely spread over space and time. Moreover, the theoretical errors (mostly of non-random nature) due to radiative transfer model are taken care by fine tuning of retrieval matrix through validation data.

General Form of Retrieval Algorithms for MADRAS

The MADRAS retrieval algorithms for various geophysical parameters would have the following general form:

$$G = c_o + \sum_{i=1}^{N} c_i \bullet f\left(Tb_i\right)$$

where, G = Desired geophysical parameter (WS, IWV, CLW), and c_o & c_i = retrieval coefficients for parameter G for i^{th} channel

Post-Launch Scenario

After MT-MADRAS is launched and the collocated *in situ* data are available, we will calibrate the pre-launch algorithm by making small adjustments to the coefficients of the retrieval algorithms presented in section 3.5. This will be carried out based on validation results.
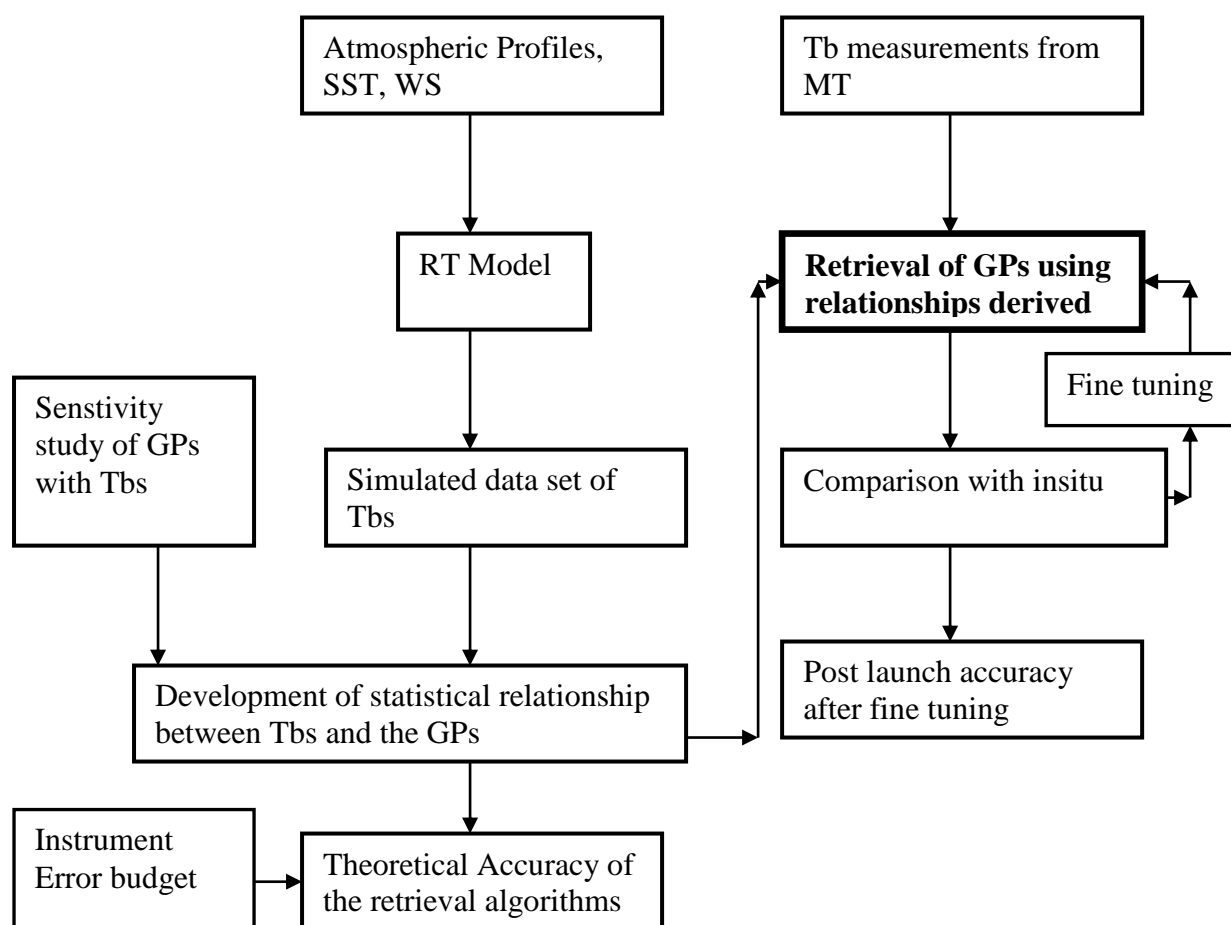
3.6.2 Flow chart

Fig. 3

3.7 Outputs

The output units, range and also the theoretical accuracy based on simulation results is as follows:

Table -5

Parameter	Unit	Min	Max	Accuracy	Resolution
IWV	gm cm^{-2}	0	10	0.48 g/cm2	Pixel
WS	m s^{-1}	0	25	1.60 m/s	Pixel
CLW	mg cm^{-2}	0	600	5.32 mg/cm2	Pixel

3.7.1 Format of the output and the domain

The output format is as follows (Table 6):

Table -6

Name and Description	Type value
Output file name	Same as input file name with extension replaced by "gp.txt"
Output file containing Latitude, longitude, day, hour, min, seconds, CLW, TPW, WS and Flag	Latitude, longitude, day, hour, min, seconds from input file CLW range 0-600 mg cm^{-2}, TPW range > 0-10 g cm^{-2}, WS range > 0 – 25 m s^{-1}, Possible Flag values: 0: good retrievals with ranges specified above, 1: one or more Tbs out-of range; All GPs set to -99.99, 2: Surface type not oceanic; All GPs set to -99.99, 3: Rain present; All GPs set to -99.99, 4: CLW > 50 mg cm^{-2}; TPW and WS set to -99.99, 5: CLW > 18 mg cm^{-2}; WS set to -99.99, 6: One of the GPs exceeding valid range and set to -99.99

3.8 Validation

A separate ATBD for validation is submitted. However, the limited validation (in collaboration with validation team) for fine tuning of the retrieval algorithm will be carried out and the details of which are presented below.

3.8.1 Data required

- Measurement of GPs from other satellites
- Surface insitu measurements over global oceans.

3.8.2 Method of validation

- Collocated pointwise comparison statistics to be generated.
- Histogram of GPs over given area and season to be compared.
- Variability and Trends to be studied.

3.9 Technical issues:

In this document we have provided the details of the various components of the retrieval algorithm for deriving the cloud liquid water, wind speed and integrated water vapor over oceans using MT-MADRAS channels. We hope to achieve the accuracies as provided for SSM/I. In view of our past experience of deriving the same parameters using MSMR observation, we do not foresee any practical difficulty in deriving the same using MT-MADRAS. The derived parameters need

to be validated   extensively over different regions and seasons of the year so that complete dynamic range of the parameters could be validated. We expect a separate team will be looking for the validation aspect. We, however, need their feedback for fine tuning the retrieval algorithms in the post launch phase.

3.10 Future Scope

Retrieval algorithms have to be validated and then if necessary fine tuning of the algorithms have to be carried out. This will be done by adjusting the coefficients in the D-matrix by minimizing the errors between observations and the estimations.

3.11 References

Alishouse, J.C., S. Synder, J. Vongsathorn, and R.R. Ferraro, Determination of oceanic total precipitable water from the SSM/I, *IEEE Trans. Geoscience and Remote Sensing*, *28*, 811-816, 1990.

Desbois, M, 1999, Megha-Tropiques: Science objectives and general mission requirements, Proc. of Megha-Tropiques: First science workshop, Eds., Narayanan, M S, Manikiam, B, and Gairola R M, 19-22 May 1999, ISRO-HQ, Bangalore, pp 1.1-1.7.

Ferraro R R, F Weng, N C Grody, and A Basist, 1996, An eight-year (1987-1994) time series of rainfall, clouds, water vapour, snow cover and sea ice derived from SSM/I measurements, *Bulletin of American Meteorological Society*, **77 (5)**, 891-905.

Ferraro R R, and G F Marka, 1995, The development of SSM/I rain rate algorithms using ground-based radar measurements, *Journal of Atmospheric and Oceanic Technology*, **12**, 755-770.

Gairola, R. M., A. K. Varma, S. Pokhrel and V. K. Agarwal, Sensitivity of Brightness Temperatures to the Oceanic Surface Roughness and Rainfall for the TRMM and IRS-P4-MSMR Radiometric Channels over the Indian Ocean, *Indian Journal of Radio and Space Physics*, 33, pp 61 -70, 2004.

Gohil, B.S., A.K. Mathur and A.K. Varma, A non-statistical algorithm for geophysical parameter retrieval from microwave radiometer onboard Oceansat-1 and DMSP satellite, Proc. of TROPMET-2000, Ed. by Joseph et al., pub. by IMS, Cochin Chapter, 1-4 Feb., 2000, Cochin Univ., 286-290, 2000a.

Gohil, B.S., A.K. Mathur and A.K. Varma, Geophysical Parameters Retrieval over Oceans from IRS-P4 MSMR, Proc. of Pacific Ocean Remote Sensing Conference (PORSEC-2000), 5-8 Dec, 2000 at NIO, Goa, 207-211, 2000b.

Goodberlet, M.A., C.T. Swift, and J.C. Wilkerson, Remote sensing of ocean surface winds with the SSM/I, *J. Geophys. Res., 94*, 14547-14555, 1989.

Grody, N.C, 1991, Classification of snow cover and precipitation using Special Sensor Microwave Imager (SSM/I), *Journal of Geophysical Research*, **96**, 7423-7435.

Guilliou, C, W Ellison, L Eymard, K Lamkaouchi, C Prigent, G. Delbos, G Balana, S A Boukabara, Emissivity modeling in Microwave, Radio Science, 33, 649-667, doi: 10.1029/97RS02744, 1998.

Liu, G, A fast and accurate model for Microwave Radiance calculations, J. Meteorol. Soc. Japan, 76 (2), 335-345, 1998.

Paris, J.F., (1971), Transfer of thermal microwave atmosphere in the I and II, Department of Meteorology, Texas A& M university, Texas.

Pokhrel, S., A. K. Varma, R. M. Gairola, , Vijay K. Agarwal, Distribution and intraseasonal variability of rain over Indian Oceanic region from Indian Remote Sensing Satellite IRS-P4 Multifrequency Scanning Microwave Radiometer, *Journal of Geophysical Research*, 108 (C10), 3314, doi:10.1029/2003JC001886, 2003.

Rosenkranz, P. W., Absorption of microwaves by atmospheric gases, Chapter-2 and Appendix, in Atmospheric Remote Sensing by Microwave Radiometry, M. A. Janssen, Ed, Wiley, New York, 1993.

Rosenkranz, P.W., Water vapor microwave continuum absorption: A comparison of measurements and models, *Radio Science*, 33(4), 919-928, 1998.

Varma, A.K., R.M. Gairola, A.K. Mathur, B.S. Gohil and V.K. Agarwal, Intercomparison of IRS-P4-MSMR derived geophysical products with DMSP-SSM/I and TRMM-TMI finished products, *Proceedings of Indian Academy of Sciences – Earth and Planetary Sciences*, 111 (3), 247-256, 2002.

Varma, A.K., R.M. Gairola, Samir Pokhrel, A.K. Mathur, B.S. Gohil and V.K. Agarwal, Rain Rate Measurements over global oceans from IRS-P4 MSMR,

Proceedings of Indian Academy of Sciences – Earth and Planetary Sciences, 111 (3), 257-266, 2002.

Varma, A K**,** B S Gohil, R M Gairola and P K Pal, A new radiative transfer based rain retrieval algorithm for rain identification and measurement from MT-MADRAS: Initial Results, internal report no.: SAC/EPSA/AOSG/MT/SR/76/2011, p 26., 2011.

Varma, A.K., Samir Pokhrel, Rakesh Mohan Gairola, and Vijay K. Agarwal, An Empirical Algorithm for Cloud Liquid Water From MSMR and Its Utilization in Rain Identification, IEEE Transactions on Geosciences and Remote Sensing, 41 (8), 1853-1858, 2003.

Varma, A. K., S. Pokhrel, R. M. Gairola and V. K. Agarwal, Study of geophysical parameters associated with the Orissa super cyclone using active and passive microwave remote sensing measurements, *International. Journal of Remote Sensing*, 27 (18), doi: 10.1080/01431160410001705060, 3753-3765, 2006.

Wentz, F. J., A well-calibrated ocean algorithm for special sensor microwave / imager, *Journal of Geophysical Research*, 102 (C4), 8703-8718, 1997.

Wilheit, T. T., and Chang, A. T. C., An algorithm for retrieval of ocean surface and atmospheric parameters from the observations of the scanning multichannel microwave radiometer, *Radio Science*, 15 (3), 525-544, 1980.

4.0 Retrieval of Humidity profiles from SAPHIR

4. Retrieval of Humidity Profiles from SAPHIR

4.1 Algorithm Configuration Information

4.1.1 Algorithm Name

Humidity profile

4.1.2 Algorithm Identifier

ISRO_MT_HUMP_A001

4.1.3 Algorithm Specification

Version	Prepared by	Description
2.0	A.K. Mathur and B.S. Gohil	Humidity profile Baseline Document
3.0	A.K. Mathur, R.K.Gangwar and B.S. Gohil	Revised inversion technique for humidity profile

4.2 Introduction

The Megha-Tropiques (MT) satellite is designed to study the impact of water cycle on atmospheric climate processes and energy exchanges over the Tropics. Megha-Tropiques was launched into a circular 867-kilometer orbit inclined at 20 degrees to the equatorial plane on 12th October 2011. From this orbit; the satellite is able to collect frequent data over the Inter-tropical Convergence Zone to complement and augment those obtained by satellites in geostationary and polar orbits. The MT satellite payloads are high-technology sensors viz. Microwave Analysis and Detection of Rain and Atmospheric Structures (MADRAS), a millimeter wave humidity profiler (SAPHIR), an optical-IR radiometer for radiation budget (ScaRAB) and a radio occultation sensor (GPS-ROS). All the sensors have been integrated with IRS platform and primarily developed under ISRO-CNES joint collaboration.

4.2.1 Overview and background:

The Sondeur Atmosphérique du Profil d'Humidité Intertropicale par Radiométrie (SAPHIR) instrument is developed by IPSL and Observatoire de Paris as part of the MEGHA-TROPIQUES payload to study the vertical distribution of water vapour in the tropical troposphere, with two specific objectives:

1. Analysis of the diurnal cycle of the water vapour distribution, to evaluate the vertical   transports associated with convective structures at the mesoscale and the large scale, and to understand the scale-to-scale interactions in the meridional flux
2. Study of the role of the space-time distribution of humidity on the development of deep convection.

An additional aim is to improve parameterizations of humidity related processes in AGCM. The need for such an instrument on the Megha Tropiques platform was driven by the following main reasons:

a) Scarcity of accurate and frequent water vapour profile measurements in tropical latitudes for studying convective system life cycle.

b) Existing and other future sounders are planned to be onboard polar orbiting satellites   leading to heterogeneous data.

4.2.2   Objectives

- To retrieve humidity profile in 6 layers of the atmosphere from 1000 to 100 mb.
- To validate the retrieved profiles with concurrent radiosonde, satellites observations and NWP model fields.
- To improve the retrievals based on the validation feedback.

4.3   Instrument characteristics:

Six SAPHIR channels are centered on major water vapour absorbing band at 183.31 GHz. The following table shows the details of its bandwidths etc.

Table1: SAPHIR Channels characteristics

Channels	Central nominal frequencies (GHz)	Nominal Bandwidth (MHz)	Lower nominal bandwidth (GHz)	Upper nominal bandwidth (GHz)
S1	183.31 ± 0,2	200	183.010 - 183.210	183.410 - 183.610
S2	183.31 ± 1.1	350	182.035 - 182.385	184.235 - 184.585
S3	183.31 ± 2.8	500	180.260 - 180.760	185.860 - 186.360
S4	183.31 ± 4.2	700	178.760 - 179.460	187.160 - 187.860
S5	183.31 ± 6.8	1200	175.910 - 177.110	189.510 - 190.710
S6	183.31 ± 11	2000	171.310 - 173.310	193.310 - 195.310

4.4   Inputs:

4.4.1   Static Data

Parameter	Resolution	Accuracy	Source
Land /Sea Mask	Pixel (~4 km)	1 pixel	USGS

4.4.2 Image and preprocessing data (Dynamic)

Parameter	Resolution	Quantization	Accuracy	Source
Radiometric and geometric corrected brightness temperatures of 6 SAPHIR channels	Each pixel /Grid	16-bit	<1K	Derived from raw data by DP
Geolocation of all the SAPHIR channels	Each pixel/ Grid	16-bit	1 pixel	Derived by DP
Geolocated Total Water vapour Content from MADRAS	Each Pixel/ Grid	16-bit		Derived by MADRAS Algorithm
Quality Flag(surface, geo-location quality, BT validitity)	Each Pixel	16-bit		Provided by DP

4.5 Algorithm functional specifications

4.5.1 Basic principle

The scientific objective of SAPHIR calls for determination of humidity with an accuracy of 10 to 20% in 6 layers of the troposphere with 10 km of spatial resolution. For realizing that goal, it is necessary to choose channels for which the atmospheric contribution to the radiance comes from different levels of the troposphere. This can be obtained by sampling an absorption line of water vapour by channels more or less close to the centre of the line. A candidate line, already chosen for other instruments, is the line at 183.3 GHz. It is possible to get contribution functions peaking from heights of 2 km up to 12 km in tropical atmospheres. However, the width of the contribution functions makes it redundant to use more than 5 channels. A sixth complementary channel, in a window region, has to be used to correct for the surface effects in the lower channels.

The SAPHIR humidity sounder operates at six channels around 183.31 GHz designated as S_1, S_2, S_3, S_4, S_5 and S_6. given in Table-1.The final selection of layers is carried out by first building a learning data base, consisting of meteorological profiles, and brightness temperatures simulated by running a radiative transfer model on the profiles; then a multiple regression inversion scheme is applied to retrieve the humidity in each layer.
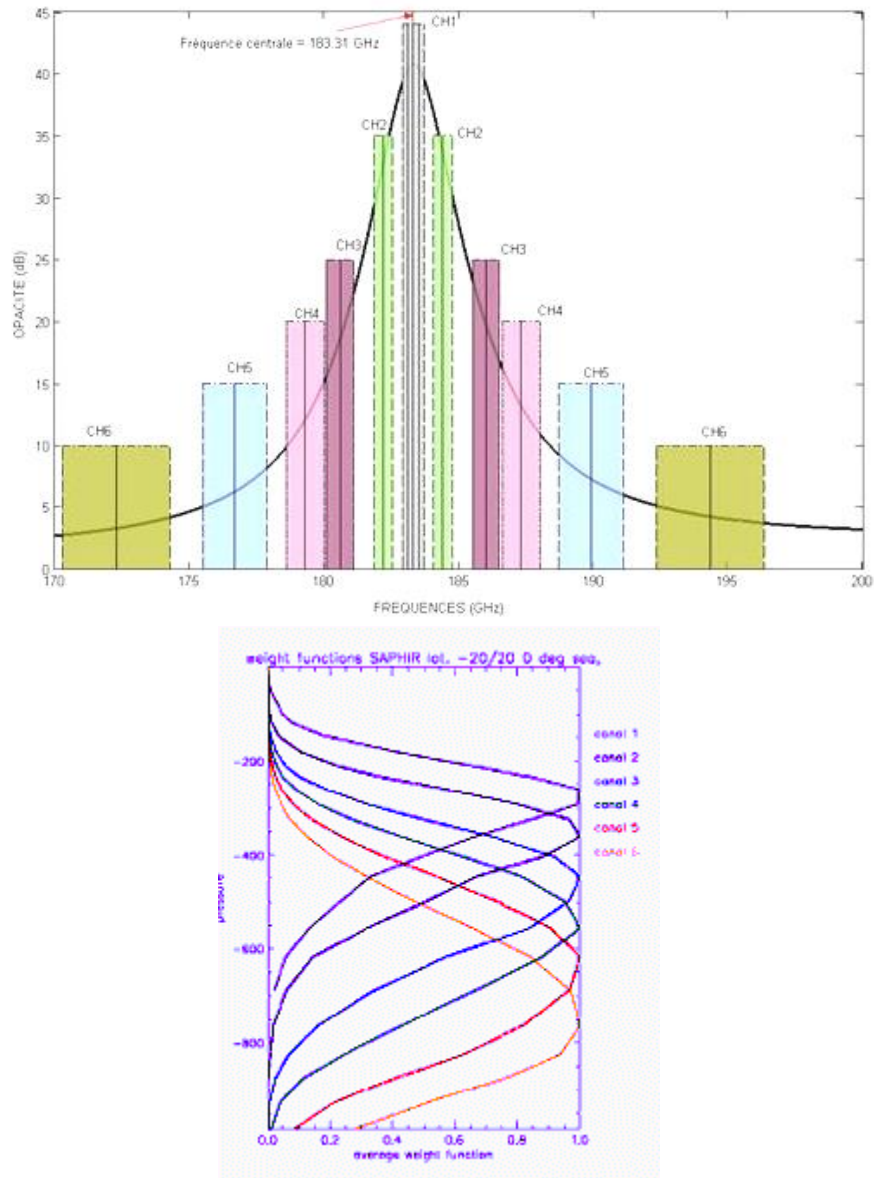
Figure 1b: Weighting functions of the 6 SAPHIR channels for a mean tropical atmosphere over sea, at nadir. Channels are numbered as shown on figure1a

4.5.1.1 Radiative Transfer Model

For a non-scattering atmosphere under LTE, total brightness temperature received by an earth-viewing microwave radiometer

$$TB(\vartheta,\theta,p) = T_s\varepsilon(\vartheta,\theta,p)\tau(\vartheta,\theta) + TB_{up}(\vartheta,\theta) + TB_{dn}(\vartheta,\theta)\{1 - \epsilon(\vartheta,\theta,p)\}\tau(\vartheta,\theta)$$

(1)

Where

$$\tau(\upsilon,\theta) = \exp\{-\sec\theta\int_0^\infty \alpha(\upsilon,z)\partial z\}$$
(2)

$$TBdn(\upsilon,\theta) = \sec\theta \int_0^\infty T(z).\alpha(\upsilon,z).\tau(\upsilon,\theta,0-z)\partial z \qquad (3)$$

$$TBup(\upsilon,\theta) = \sec\theta \int_0^\infty T(z).\alpha(\upsilon,z).\tau(\upsilon,\theta,z-\infty)\partial z \qquad (4)$$

and

$$\tau(\upsilon,\theta,z1-z2) = \exp\{-\sec\theta \int_{z1}^{z2} \alpha(\upsilon,z)\partial z\} \qquad (5)$$

Where α, τ are atmospheric absorption and transmittance, respectively, Ts, ε are sea surface temperature and emissivity, θ, υ, p are incidence angle, frequency of SAPHIR channel and polarization. Tb$_{up}$, TB$_{dn}$ are upwelling and down-welling atmospheric brightness temperatures. The models used are those of Liebe (1993) for atmospheric absorption, Hollinger (1973) for calm, Stogryn (1972) for wind roughened and Wilheit (1979) for foam covered sea surface emissivity, respectively. Low frequency wing of SAPHIR channels have been considered for the simulations of brightness temperatures.

For the microwave frequencies in the resonance region of dominant absorbers like water vapour and oxygen, the transmittance is very low or negligible so that the contribution to the total radiation to the radiometer by reflected down-welling and surface radiations becomes negligible. Therefore, the total brightness temperature is expressed as

$$TB(f,\theta) = sec\theta \int_0^\infty T(z) \propto (f,z)\tau(f,\theta,z-\infty)\delta z \qquad (6)$$

The product of absorption due to a thin atmospheric layer and the transmittance of the overlying atmosphere is known as the weighting function as given below

$$TB(f,\theta) = sec\theta \int_0^\infty T(z)W(f,\theta,z)\delta z$$

$$(7)$$

with

$$W(f,\theta,z) = \propto (f,z)\tau(f,\theta,z-\infty)$$

The profile of weighting function with altitude is characterized by the absorption profile for a specific frequency. The weighting function profile has a peak at a particular altitude for a particular frequency in resonance region. This implies the maximum sensitivity of a channel at the peak altitude of weighting function. This forms the basis for the sounding of the atmosphere at various altitudes using different channels in the resonance region. On the other hand, the radiation received by the radiometer is the weighted contribution by different layers of the atmosphere with maximum contributions from the layers having peak weighting function. The peak of the weighting function shifts towards higher altitude as the channel frequency nears the resonance line of an absorber. Contrary to it, the peak of weighting function shifts towards surface for transparent or window channels and the atmospheric contributions also reduce to greater extents. The window channels are used for surface sensing.

4.5.1.2 Retrieval techniques:

The sensitivity of simulated brightness temperatures on humidity has been studied under varying atmospheric conditions. This experiment is useful in selecting the atmospheric thick-overlapping layers (TOL) influencing maximum number of channels to be considered for better retrievals. Additionally, these TOL are also innovatively utilized to derive humidity for thin-isolated layers (TIL) which otherwise will have large retrieval errors when directly derived from the channel brightness temperatures (due to broad overlapping nature of channel's Weighting Functions (WFs) as shown in Figure 1b). Retrieval has been performed for the 7 TOL's lying between the pressure values (1000-550) mb, (1000-400) mb, (850-400) mb, (850-250) mb, (700-250) mb, (700-100) mb and (550-100) mb respectively on the basis of their sensitivity with SAPHIR channels' brightness tempratures. From these seven TOL's, the LARH for six TIL's lying between pressure values (1000-850) mb, (850-700) mb, (700-550) mb, (550-400) mb, (400-250) mb, and (250-100) mb have been derived.

Definitions of the TOL and TIL are given below.

The layer-average relative humidity (LARH) for TOL is the relative humidity (RH) averaged with respect to logarithm of pressure over a layer between two pressure limits "p1" and "p2" as defined below

$$TOL_{p1,p2} = \int_{\ln (p1)}^{\ln (p2)} RH(p)\delta(\ln (p)) / \{\ln(p1) - \ln(p2)\} \qquad (8)$$

As mentioned above, thin-isolated layers (TILs) have also been derived from two Thick-overlapping layers (TOLs) as follows. From known LARH values for two TOLs with pressure levels "p1" to "p3" and "p2" to "p3", the LARH value for a TIL with pressure levels "p1" to "p2" can be derived as

$$TOL_{p1,p3} = \int_{\ln (p1)}^{\ln (p3)} RH(p)\delta(\ln(p)) / \{\ln(p1) - \ln(p3)\}$$

$$(9a)$$

$$TOL_{p1,p3} = [\int_{\ln (p1)}^{\ln (p2)} RH(p)\delta(\ln(p)) + \int_{\ln (p2)}^{\ln (p3)} RH(p)\delta(\ln(p))] / \{\ln(p1) - \ln(p3)\}$$

$$(9b)$$

$$TOL_{p2,p3} = \int_{\ln (p2)}^{\ln (p3)} RH(p)\delta(\ln(p)) / \{\ln(p2) - \ln(p3)\}$$

$$(9c)$$

The LARH for TIL between "p1" to "p2" is derived using expressions (9b and 9c) as

$$TIL_{p1,p2} = \left[TOL_{p1,p3} \cdot \{\ln(p1) - \ln(p3)\} - TOL_{p2,p3} \cdot \{\ln(p2) - \ln(p3)\} \right] / \{\ln(p1) - \ln(p2)\}$$

(9d)

The relationship between brightness temperature and TOL for SAPHIR channels is established as given as

$$TOL_p = A_{0,p} + A_{1i,p}(320 - TB_i) + A_{2i,p}(320 - TB_i)^2$$

(10)

Where TOL is the layer averaged relative humidity in percent, $A_{0,p}$ is the retrieval constant for p^{th} layer, $A_{1i,p}$ and $A_{2i,p}$ are retrieval coefficient for i^{th} channel, TB_i is brightness temperatures of ith SAPHIR channel with six channels. The coefficients have been established using the simulated BT from the simulated clear sky atmospheres mentioned above. The noise in all BT's has been introduced as per the noise characteristics of SAPHIR instrument.

TIL are derived from TOL from the following relationship

$$TIL = A_0 + A_{1,i} \sum_{i=1}^{2} TOL_i$$

(11)

Where, these TOL's are those having the desired TIL as their difference.
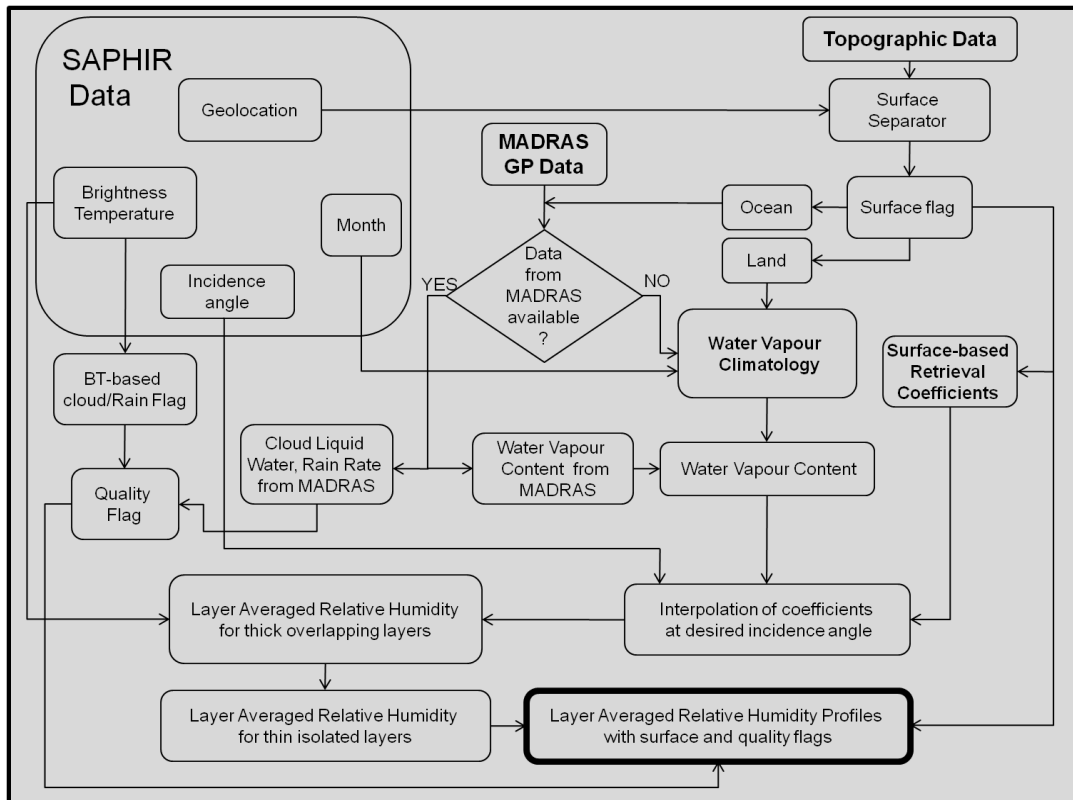
4.5.2 Flow-chart:

Figure 2: Flow chart of the Retrieval Algorithm for Humidity profile from SAPHIR

4.6 Operational implementation

Operational implementation of the retrieval scheme for SAPHIR Sounder includes the following procedures:

- Development of forward radiative transfer model to compute SAPHIR channels brightness temperatures given various atmospheric and surface conditions as input.
- Identification of cloud and rain free pixels
- Derivation of retrieval coefficients for layer averaged relative humidity at different layers from SAPHIR brightness temperatures using statistical regression.

4.7 Outputs

LARH (TIL)	Unit	Min	Max	Expected Accuracy (%)	Resolution-horizontal (km)
Layer-1(1000-850) mb	%	0.1	100	~20	10
Layer-2 (850-700) mb	%	0.1	100	~20	10
Layer-3 (700-550) mb	%	0.1	100	~20	10
Layer-4 (550-400) mb	%	0.1	100	~20	10
Layer-5 (400-250) mb	%	0.1	100	~20	10
Layer-6 (250-100) mb	%	0.1	100	~20	10
Layer-1 (1000-850) mb	%	0.1	100	~20	10

4.8 Validation

Validation of the derived humidity profiles will be done using all the available data from radiosonde, special cruises over oceans and available similar products from various satellite missions.

4.8.1 Data required:

Radiosonde and ship data for validation should consists of following parameter
- Station/Ship ID
- Location of the measurement
- Time of the measurement
- Relative humidity in %
- Height/pressure at which measurement is taken
- Air Temperature at the same height

- Instrument accuracy of humidity.

4.8.2   Methods of validation

From the observed profiles of humidity for clear sky conditions, brightness temperatures corresponding to SAPHIR channels will be computed with the help of radiative transfer model used in the retrieval algorithm. The computed brightness temperatures are analysed with SAPHIR-observed brightness temperatures to estimate the bias (slope and intercept of the linear regression equation) for each of the sounder channels. These bias-corrections will be implemented in the regression retrieval routines to remove the bias between sounder observations and the radiative transfer model computations.

4.9   Future scope:

The present study does not include the sensitivity of SAPHIR channels to land emissivity variations and clouds. Inclusion of such cases will definitely improve the quality of humidity profiles. In order to minimize the surface contribution in the lower frequency SAPHIR channels inclusion of 150 GHz brightness temperature from MADRAS is also desirable that will be taken up in future..

4.10   References

1. Gohil, B.S., B.G. Vasudevan, S.K. Basu, A.K. Mathur and V.K. Agarwal (2001), "Simulation studies of humidity profiles retrieval from Megha-Tropiques SAPHIR", presented at 2nd ISRO-CNES Science Workshop on Megha-Tropiques held during July 1-6, 2001, PARIS, France.

2. Gohil, B.S., and A.K. Mathur(2005), "Atmospheric Humidity Profile Retrieval Algorithms for Megha-Tropiques SAPHIR: A simulation Study and Analysis of AMSU-B Data", presented at 3rd ISRO-CNES Science Workshop on Megha-Tropiques held during October 17-20, 2005, Ahmedabad

3. Gohil, B.S., A.K. Mathur, A. Sarkar and Vijay K. Agarwal (2006), 'Atmospheric humidity profile retrieval algorithms for Megha-Tropiques SAPHIR: A simulation study and analysis of AMSU-B data', Proceedings of SPIE Conference on Remote Sensing and Modeling of the Atmosphere, Oceans, and Interactions, edited by T N. Krishnamurti, B. N. Goswami and T Iwasaki, Vol. 6404, 13-17 Nov. 2006.

4. Hollinger J.P. (1973), "Microwave properties of calm sea", NRL Report No 71-71102-2, Naval Research Laboratory, Washington. D.C.

5. Liebe, H.J., G. A. Hufford, and M. G. Cotton (1993), "Propagation modeling of moist air and suspended water/ice particles at frequencies below 1000 GHz", Proceedings of AGARD Conference on Electromagnetic Wave Propagation, pp-3/1-10, Palma De Mallorca, Spain.

6. Rosenkranz P W (2001),'Retrieval of temperature and moisture profiles from AMSU-A and AMSu-B measurements', IEEE Trans. Geo. Rem.

Sens.,vol 39, 2429-2435 pp.

7. Sohn, B. and Chung E, (2003) "Estimating Upper-Tropospheric water vapour from SST-2 satellite measurements", Jou. App. Met., Vol 42, pp 488-504.

8. Spencer, R.W. and W.D. Braswell (1997), "How dry is the tropical free troposphere? Implications for global warming theory", Bull. American Meteor. Society, vol 78, No. 6, pp 1097-1106.

9. Stogryn, A., (1972) "The emissivity of sea foam at microwave frequencies", Jou. Geophys. Research, vol 77, pp 1650-1666.

10. Wang J R, J D Spinhirne, P Racette, L A Chang and W Hart(1997), ' The effect of clouds on water vapour profiling from the millimeter-wave radiometric measurements', J App. Met., Vol.36, 1232-1244 pp.

11. Wilheit, T.T (1979), "A model for microwave emissivity of the oceans surface as function of wind speed", IEEE Trans. Geosci. Elec., GE-17, pp 244-249.

12. Wilheit T T (1990), 'An algorithm for retrieving water vapor profiles in clear and cloudy atmospheres from 183 GHz Radiometric measurements: Simulation studies', J. App. Met.,Vol. 29, 508-515 pp.

5.0 Top-of-Atmosphere Radiative Flux from ScaRaB

5 Top-of-Atmosphere Radiative Flux from ScaRaB

5.1 Algorithm configuration information

5.1.1 Algorithm name:
Top of Atmosphere Flux Computation (TOA_FLUX)

5.1.2 Algorithm Identifier:
ISRO_MT_TOAFLUX_A001

5.1.3 Algorithm Specification

Version	Prepared by	Description
3.0	V. Sathiyamoorthy Bipasha Paul Shukla	ATBD for top of atmosphere radiance-to-flux computation

5.2 Introduction

An understanding of the radiation budget of the earth is fundamental because the weather/climate system is a heat engine, with absorbed solar radiation being the energy source and Earth-emitted radiation being the energy sink necessary to drive the system. Earth Radiation Budget studies are of paramount importance in the context of global climate change. The delicate balance of the incoming and the outgoing radiation, which is being disturbed by anthropogenic activities, mark their signatures in the top of atmosphere radiation budget quantities. Top of atmosphere radiation budget quantities can be estimated from satellites using well-calibrated broadband radiometers.

Scanner for Radiation Budget (ScaRaB) onboard Megha-Tropiques is a 4-channel cross-track scanning radiometer. The four channels include two broad spectral bands (Channel-2 and Channel-3) from which the reflected shortwave and emitted longwave radiances are derived and two narrow bands (Channel-1 and Channel-4) one corresponding to the infrared atmospheric window, other to the visible (green to red) portion of the solar spectrum (Table.1). Purpose of keeping the two narrow band channels are: (i) R&D activities and (ii) estimate the errors associated with the narrow band to broad band extrapolations.

Table-1 ScaRaB Channels

Channel No.	Description	Wavelength Range
1	Visible (VIS)	0.55 - 0.65 μm
2	Solar (SW)	0.2 – 4.0 μm
3	Total (T)	0.2 – 100 μm
4	IR Window (IR)	10.5 – 12.5μm

Satellite measurement of the earth–atmosphere radiations are usually confined to certain local times and specific directions of view depending on orbital constraints

and instrument scanning capabilities. Due to the smaller spatial view of the ScaRaB, only limited angular coverage is possible by each observation. In the case of ScaRaB, the direct measurement is radiance while the desired measurement is radiative flux at the top of atmosphere. Derivation of the radiative flux using the ScaRaB radiance observations then requires the use of measured satellite radiances and assumptions about the anisotropy of the earth's radiation field. The primary modification of the earth's anisotropy is caused by the variations in cloud properties. In this document details about the ScaRaB/Megha-Tropiques data processing system that can compute top of atmosphere shortwave (SW) and Longwave (LW) fluxes from measured radiances is described.

5.2.1 Overview and Background:

The ScaRaB/Megha-Tropiques data processing system corresponds to the ERBE-like data processing system, already used and assessed by the former ERBE, ScaRaB and CERES experiments. In this system, the 'maximum likelihood estimation' algorithm (Wielicki and Green, 1989) is used for scene identification. The 12-scene classification is based on five geo-types [ocean, land, snow-ice, desert and coast] and four cloud types [clear, partly cloudy, mostly cloudy and overcast]. The raw radiances are first corrected for spectral filtering effects as a function of identified scene. Next scene-type dependent angular correction models (anisotropic factor from Suttles et al, 1988; 1989) are used to deduce the SW and LW fluxes of the pixel as a function of measured radiances.

Three important steps involved in the ScaRaB radiance to flux computation are:
1. Spectral correction
2. Scene Identification and
3. Flux computation (by applying scene-type dependent ADM).

5.2.1.1 Spectral Correction

The calibrations of the filtered radiances L_T^f and L_{SW}^f are normalized to precise radiation sources: blackbodies at temperature respectively 310 K and 5800 K. Then the unfiltered radiances are equal to filtered radiances only if the observed targets have similar or proportional emission spectra. Otherwise the unfiltered radiances are calculated from the filtered radiances

$$L_{scene} = \frac{L_{scene}^f}{F_{scene}} \qquad\qquad -- (1)$$

where F_{scene} is the filtering factor, varying around 1 according to the spectral shape or colour of the scene.

5.2.1.2 Scene Identification

Unlike the CERES instrument on TRMM, Aqua and Terra missions, the ScaRaB/MeghaTropiques will not have an imager payload for scene identification. To identify the scene, the indirect ERBE scene identification method (Wieliecki et al., 1989) will be utilized. This is a statistical approach

called Maximum Likelihood Estimation (MLE) technique and uses only the unfiltered L_{LW} and L_{SW} radiances measured by ScaRaB for scene identification.

5.2.1.2.1 ERBE Angular Model

Both the scene identification and the flux computation use the ERBE Angular Dependence Model (ADM) generated by Suttles et al. (1989). From statistical analysis of satellite measurement (mainly seven months of Nimbus 7 radiance measurements), the radiance anisotropy is described for 12 scene types, combination of 5 geo-types and 4 cloud cover categories (Table 2). In the LW, the ADM depends on latitude and season. The ADM are not continuous functions of the angles, but discrete values corresponding to the angular intervals.

Table-2 ERBE 12-Scene types

No.	Scene Type	Cloud Fraction (%)
1	Clear Ocean	0-5
2	Clear Land	0-5
3	Clear snow/ice	0-5
4	Clear Desert	0-5
5	Coastal	0-5
6	Partly cloudy ocean	5-50
7	Partly cloudy land	5-50
8	Partly cloudy coastal	5-50
9	Mostly cloudy ocean	50-95
10	Mostly cloudy Land	50-95
11	Mostly cloudy coastal	50-95
12	Overcast	95-100

In the following, subscript Mod stands for Modelled (ADM).
R is the LW anisotropy function
ρ is the SW anisotropic function (bidirectional reflection)

The LW ADM contains:
1. Flux M_{mod} (Iscn, Colat)

2. Anisotropy function R (Iscn, θ', Colat)

3. Standard-deviation of radiances in the corresponding angular bin σ (Iscn, θ', Colat)

The SW ADM contains:
1. Albedo a_{mod} (Iscn, θ_o')

2. SW anisotropy function ρ (Iscn, θ_o', θ', φ')

3. Standard-deviation of radiances σ (Iscn, θ_o', θ', φ')

4. The LW-SW correlation coefficient

Here Iscn = scene

Colat = colatitude

θ' = view zenith angle (VZA)

θₒ' = solar zenith angle (SZA)

φ' = relative azimuth (RA)

Instead of using a_{mod} it is practical to define the angular dependence of the albedo:

$$\delta \ (Iscn, \theta_o') = a_{mod} \ (Iscn, \theta_o')/ \ a_{mod} \ (Iscn, \theta_o'=0)$$

Where the denominator is the 'overhead' albedo or albedo for sun at zenith

5.2.1.2.2 Maximum Likelihood Estimator

From the ADM tables, the modelled radiances with their associated standard deviations can be easily calculated for the four cloud categories. In the LW/SW graph (Figure-1), the centre of the ellipse represents the average SW-LW radiances and the areas describe the standard deviation. The cloud fraction of a measurement is determined by its location on this plane. For each ScaRaB measured SW-LW pair, probabilities for being each case are calculated. The highest probability identifies the cloud fraction.
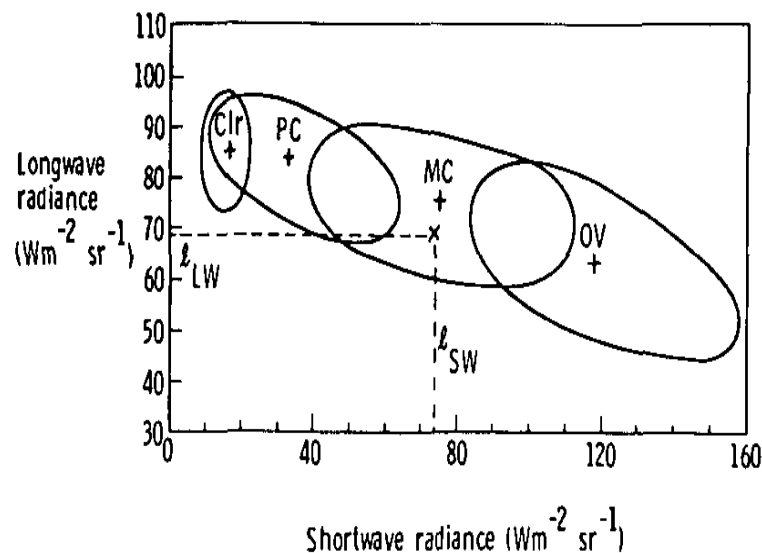

Figure-1: Equiprobability Ellipses for MLE. Clr (clear), PC (partly cloudy), MC (mostly cloudy), OV (overcast). (From Wielicki and Green, 1989).

5.2.1.3 LW Scene Identification

This scene identification is done for night-time. The algorithm proceeds with the following steps:

Step-1 Search the geographic information N_{geo}
From latitude and longitude, the following variables are searched:
N_{geo} : Geo-type (ocean, land, desert, snow-ice, coast)

M_{geo} : Outgoing clear sky flux (Wm^{-2})

For the earlier ScaRaB missions, the geo-type map was updated each month to take into account the variation of snow at high latitudes. For Megha-Tropiques such an update may be not necessary due to the negligible snow cover variation in the 30° tropical coverage belt.

The M_{geo} dataset is also defined on monthly basis. Then the M_{geo} corresponding to land and desert regions are corrected for diurnal variations.

Step-2 Compute the theoretical outgoing flux **M** from M$_{geo}$ and ADM
For each cloud category (1 to 4):

$$\mathbf{M}(Iscn, Colat) = \underline{M_{mod}}\ (Iscn, Colat)$$
$$+ F_c\ [\underline{M_{geo}(Colat, Lon)} - \ \underline{M_{mod}}\ (Ngeo, Colat)] \quad \text{---(2)}$$

where F_c is is related to the cloud fraction
$F_c = 1$ for clear
$F_c = 0.75$ for partly cloudy
$F_c = 0.25$ for mostly cloudy
$F_c = 0$ for overcast
It is easy to check:
$\mathbf{M}\ (Iscn, Colat) = \underline{M_{mod}}\ (Iscn, Colat)$ for overcast
$\mathbf{M}\ (Iscn, Colat) = M_{geo}(Colat, Lon)$ for clear sky

Step-3 Compute the theoretical LW radiance $\mathbf{L}^{LW}$

$$\mathbf{L}^{LW} = [\ R\ (Iscn, \theta', Colat) . \mathbf{M}(Iscn, Colat)\ ] / \pi \qquad \text{---(3)}$$

where R is the anisotropic factor

Step-4 Compare the measured radiance to theoretical radiance
For each cloud category (1 to 4):

Compute the probability

$$\mathrm{Pr}ob(Iscn) = \frac{\exp(\dfrac{-Q}{2})\Delta L_{Mes}^{LW}}{\sqrt{2\pi}\sigma\ (Iscn, \theta', colat)}\ AP(Iscn, Colat) \qquad \text{---(4)}$$

where AP is the a priori probability and

$$Q = \left[\frac{L_{Mes}^{LW} - \hat{L}^{LW}(Iscn, \theta', Colat)}{\sigma\ (Iscn, \theta', colat)}) \right]^2 \qquad \text{---(5)}$$

Keep the case for which Probability is the highest.

5.2.1.4 Scene Identification for day time

The algorithm is similar to night time algorithm, except it deals with the LW - SW pair instead to LW alone.

Step-1 Search the geographic information N_{geo}

From latitude and longitude, the following variables are searched:

N_{geo} : geotype (ocean, land, desert, snow-ice, coast)

M_{geo} : the outgoing clear sky flux (Wm^{-2})

a_{geo} : the clear sky albedo

The M_{geo} and a_{geo} dataset are defined on monthly basis. The M_{geo} corresponding to land and desert are corrected for diurnal variations.

Step-2 Compute the theoretical albedo $\hat{a}$ from a_{geo} and ADM

For each cloud category (1 to 4):

$$\hat{a} (Iscn, \theta_o') = a_{mod} (Iscn, \theta_o')$$
$$+ F_c [a_{geo}(Colat, Lon). \delta(\theta_o') - a_{mod} (Ngeo, \theta_o')] \quad ---(6)$$

where F_c is related to the cloud fraction, and has been defined above in the 'night time' section

It is easy to check:

$$\hat{a} (Iscn, \theta_o') = a_{mod} (Iscn, \theta_o') \quad \text{for overcast}$$
$$\hat{a} (Iscn, \theta_o') = a_{geo}(Colat, Lon). \delta(\theta_o') \text{ for clear sky}$$

Step-3 Compute the theoretical SW radiance $\mathbf{L}^{SW}$

$$\mathbf{L}^{SW} = [\rho (Iscn, \theta_o', \theta', \varphi') \hat{a} (Iscn, \theta_o')] (E_0 \cos(\theta_o') / \pi) \quad ---(7)$$

where ρ is the anisotropic bi-directional factor

Step-4 Compute the theoretical LW radiance $\mathbf{L}^{LW}$

Similarly as in the night-time section

$$\mathbf{L}^{LW} = [R (Iscn, \theta', Colat) . \mathbf{M}(Iscn, Colat)] / \pi \quad ---(8)$$

where R is the anisotropic factor

Step-5 Compare the pair of measured radiances to theoretical radiances

For each cloud category (1 to 4):

Compute the probability

$$\Pr ob(Iscn) = \frac{\exp(\frac{-Q}{2})\Delta L_{Mes}^{SW}\,\Delta L_{Mes}^{LW}}{\sqrt{2\pi}\sigma^{SW}\,(Iscn,\theta o,\vartheta,\varphi)\sigma^{LW}\,(Iscn,\theta',colat)}\,AP(Iscn,Colat) \quad \text{---(9)}$$

where AP is the a priori probability and

$$Q = \left[\frac{L_{Mes}^{SW} - \hat{L}_{SW}\,(Iscn,\theta o,\vartheta,\varphi))}{\sigma^{SW}\,(Iscn,\theta o,\vartheta,\varphi)})\right]^2 + \left[\frac{L_{Mes}^{LW} - \hat{L}_{LW}\,(Iscn,\theta',Colat)}{\sigma\,(Iscn,\theta',colat)})\right]^2 \quad \text{---(10)}$$

and keep the case for which Prob. is the highest.

5.2.1.5 Flux Computation

The flux density $F(\theta_o)$ is the integration of the radiances in the hemisphere

$$F(\theta_O') = \int_0^{\pi/2}\int_0^{2\pi} L(\theta_O',\theta',\varphi')\cos\theta'\sin\theta'\,d\theta'\,d\varphi' \quad \text{---(11)}$$

As discussed earlier, the radiance-to-flux computation is based on the 'angular dependence model' (ADM), which depends on the type of the observed scene (J). The ADM is defined by the anisotropy function R_J,

$$R_J(\theta_O',\theta',\varphi') = \frac{\pi L_J(\theta_O',\theta',\varphi')}{\int_0^{\pi/2}\int_0^{2\pi} L(\theta_O',\theta',\varphi')\cos\theta'\sin\theta'\,d\theta'\,d\varphi'} \quad \text{---(12)}$$

which yields the formula for the radiance-to-flux conversion

$$F(\theta_O') = \frac{\pi L(\theta_O',\theta',\varphi')}{R_J(\theta_O',\theta',\varphi')} \quad \text{---(13)}$$

For the LW domain, the formulas are simplified since they don't depend on the solar direction (θ_o,φ).

5.3   Inputs

5.3.1   Static Data

Parameter	Resolution	Source
Geotype [ocean, land, desert, snow-ice, coast]	2.5 Deg	ERBE
Outgoing clear-sky LW flux	-	Suttles et al. (1989)
Clear sky albedo	-	Suttles et al. (1989)

5.3.2 Shortwave ADM

For each of the twelve scene types, the SW anisotropic factor, SW Standard deviation and correlation of LW and SW are available at discrete intervals of Solar Zenith Angle (SZA), Viewing Zenith Angle (VZA) and Relative Azimuth (RA) given in Table.

Solar Zenith Angle (Deg)	Viewing Zenith Angle (Deg)	Relative Azimuth Angle (Deg)
0 - 25.84	0 - 15	0 - 9
25.84 - 36.87	15 - 27	9 - 30
36.87 - 45.57	27 - 39	30 - 60
45.57 - 53.13	39 - 51	60 - 90
53.13 - 60.00	51 - 63	90 - 120
60.00 - 66.42	63 - 75	120 - 150
66.42 - 72.54	75 - 90	150 - 171
72.54 - 78.46		171 - 180
78.46 - 84.26		
84.26 - 90.00		

5.3.3 Long wave ADM

For each of the twelve scene types, the LW anisotropic factor and LW Standard deviation are available at the following co-latitude and VZA intervals:

Co-latitude (Deg)	Viewing Zenith Angle (Deg)
0 – 18	0 - 15
18 – 36	15 - 27
36 – 54	27 - 39
54 – 72	39 - 51
72 – 90	51 - 63
90 – 108	63 - 75
108-126	75-90
126-144	
144-162	
162-180	

5.3.4   Main Input data

Parameter	Resolution	Source
Co-latitude of sample	Pixel	Level-1 file
Longitude of sample	Pixel	Level-1 file
Filtered Shortwave Radiance [$Wm^{-2}sr^{-1}$]	Pixel	Level-1 file
Filtered Synthetic LW Radiance [$Wm^{-2}sr^{-1}$]	Pixel	Level-1 file
Sample acquired time	Pixel	Level-1 file
Solar Zenith Angle	Pixel	Level-1 file
View Zenith Angle	Pixel	Level-1 file
Relative Azimuth	Pixel	Level-1 file
Quality Flag – Filtered SW (Solar) Radiance	Pixel	Level-1 file
Quality Flag – Filtered Synthetic LW Radiance	Pixel	Level-1 file

5.4   Operational implementation

The level-2 data processing system processes successively all the observations of one satellite dump (consists of few orbits) or one complete orbit data whichever is provided. It has the important module called the INV module. It does data inversion by identifying scene and computing flux.

They proceed according to the following flow-chart (Fig.2). The input is Level-1 file (output from level-0 data processing) and the output is Level-2 file (equivalent of CERES ES-8 file).

5.5   Output

Parameter	Unit	Accuracy	Resolution
Co-latitude	Deg	-	Pixel
Longitude	Deg	-	Pixel
Unfiltered SW Radiance	$Wm^{-2}sr^{-1}$	-	Pixel
Unfiltered LW (synthetic) Radiance	$Wm^{-2}sr^{-1}$	-	Pixel
SW flux	Wm^{-2}	20 %	Pixel
LW flux	Wm^{-2}	5 %	Pixel
Scene Type	-	-	Pixel

In addition to the above parameters, Solar Zenith Angle($\theta_{sun)}$, View Zenith($\theta_{view)}$, Relative Azimuth(φ) and sample acquired time are also provided.
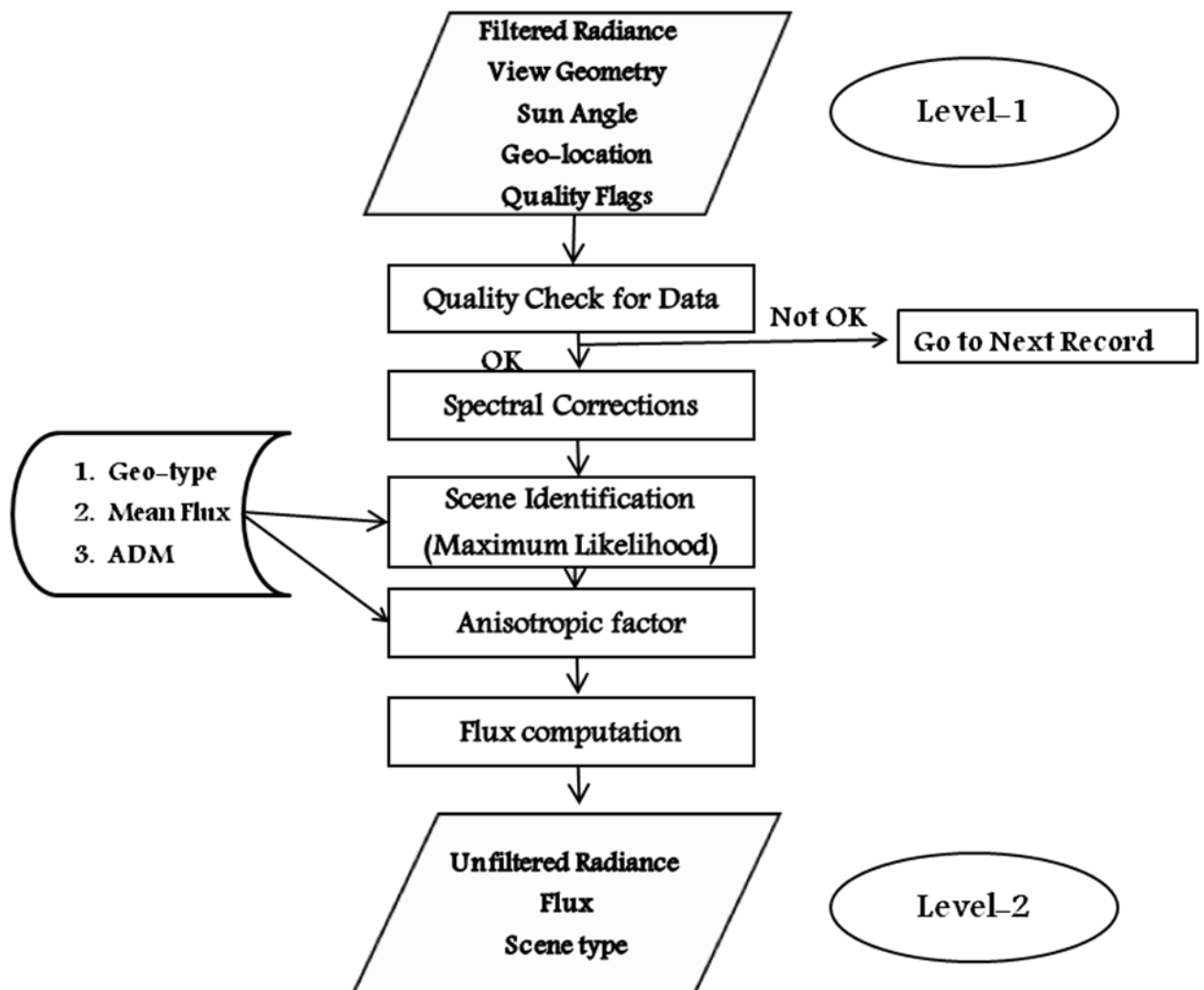
Fig. 2: Flow chart of Level-2 data processing system.

5.6   References:

1. Duvel, J. P., M. Viollier, P. Raberanto, R. Kandel, M. Haeffelin, L. A. Pakhomov, V. A. Golovko, J. Mueller,R. Stuhlmann, and the International ScaRaB Scientific Working Group, 2001: The ScaRaB-Resurs Earth Radiation Budget Dataset and First Results. *Bull. Amer. Meteor. Soc.*, **82**, 1397-1408.

2. Suttles, J. T., and Coauthors, 1988: *Angular Radiation Models for the Earth–Atmosphere System.* Vol. 1. NASA, 147 pp.

3. ——, R. N. Green, G. L. Smith, B. A. Wielicki, I. J. Walker, V. R. Taylor, and L. L. Stowe, 1989: *Angular Radiation Models for the Earth–Atmosphere System.* Vol. II. NASA, 87 pp.

4. M. Viollier, P. Raberanto and V. Sathiyamoorthy 2007: *MeghaTropiques – ScaRaB flux computation: summary of the former data processing.* LMD Report, LMD, Ecole Polytechnique, Palaiseau Cedex (France).

5. Wielicki, B. A., and R. N. Green, 1989: Cloud identification for ERBE radiative flux retrieval. *J. Appl. Meteor.,* **28,** 1133–1146.

6.0 Temperature and Humidity Profiles from ROSA

6 Temperature and Humidity Profiles from ROSA

This section deals with the description of retrieval algorithm developed in-house for deriving profile of temperature and water vapor partial pressure from profile of refractivity derived in turn from raw measurements by GPS-based Radio Occultation sensor-ROSA on board MEGHA-TROPIQUES satellite.

6.1 Algorithm Configuration Information:

6.1.1. Algorithm Name
Retrieval of profiles of temperature (T), Pressure (P) and water vapor partial pressure (e) from ROSA derived refractivity profiles for the neutral atmosphere using a conventional iteration-based method.

6.1.2 Algorithm Identifier
ISRO_MT_OSM_A001

6.1.3 Algorithm Specification

Version	Prepared By	Description
3.0	Abhineet Shyam and B S Gohil	ATBD for Temperature and water vapor partial pressure retrieval from ROSA-derived refractiv--ity

6.2 Introduction
Temperature, pressure and humidity information are, inter-alia, vital information as to the state of the atmosphere, of critical importance to studies of weather and climate. GPS-Radio Occultation (GPS-RO) based retrieval of these atmospheric parameters is a relatively novel approach to limb sounding technique, with the constellation of GPS satellites and deployed Low Earth Orbit (LEO) receiver/s constituting its gross measurement system.

ROSA, onboard MEGHA-TROPIQUES, is the deployed GPS receiver in context tracking L-band dual-frequency signals transmitted by GPS satellites.

Operating frequency	Specification
L1 C/A code signal	1575.42 MHz
L1 P-code signal	1575.42 MHz
L2 P-code signal	1227.60 MHz

The orbital specification of Megha-Tropiques combined with ROSA receiver specification, is likely to result in occultation event frequency in excess of 500 per day with spatial coverage from 30S – 30N latitude. Multiple space-based GPS receivers are configured to give increased occultation events. Currently, COSMIC, which is a constellation of six receivers, is a multiple-receiver mission yielding between 1800-2500 occultations per day and a dense coverage of mid-latitude region.

This document is primarily concerned with the delineation and description of conceptual constructs in the retrieval of afore-mentioned geophysical parameters

from GPS-RO derived refractivity and the associated elements in development of the algorithm for the same and its operational implementation. A meaningful starting point for this purpose is the relationship, also called forward model, between the derived refractivity and geophysical parameters to be retrieved viz. temperature (T), pressure (P) and water vapor partial pressure (e). However, a brief overview of the theoretical background of the GPS-RO technique, beginning with the raw measurements to the derivation of refractivity, is given for greater comprehension and continuity.

6.2.1 Theoretical Background

The basic observables of this technique are the phase and amplitude of the dual-frequency signals transmitted by a GPS satellite and received by the LEO receiver in an occulting geometry as depicted in Fig.1. The recorded phase, corresponding to a single frequency, is the sum of vacuum phase and an excess phase, due to the intervening atmosphere. Obtaining excess phase delay involves precise measurement of GPS and LEO satellite orbits (position and velocities) and phase delays of GPS signals (at L1 and L2 frequencies) to a very high accuracy. From the time series of excess phase delay (obtained after removing vacuum phase delay from measured phase delay) and position and velocities of GPS and LEO, bending angle profile as a function of impact parameter is computed.
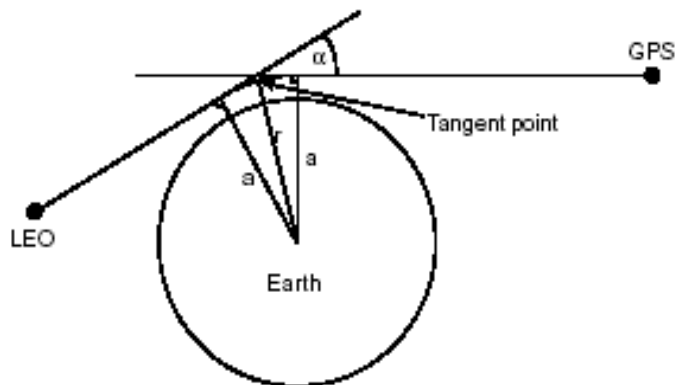

Figure 1. A schematic diagram of radio occultation sounding geometry

The main steps involved in the retrieval of refractivity and related atmospheric parameters are as follows (Steiner et al., 1999):

1. Calculation of the atmospheric bending angle profile from the observed L1/L2 excess phase path time series (including dual-frequency ionospheric correction).
2. Retrieval of the refractive index profile from the atmospheric bending angle profile and conversion to refractivity profile.
3. Calculation of pressure, and temperature based on the refractivity profile (assuming dry air). The pressure and temperature so calculated are the dry pressure and dry temperature, distinct from real pressure and temperature in the water vapor dominant region (i.e. lower troposphere).
4. Deriving water vapor partial pressure with a simultaneous refinement of dry temperature and pressure to get real state parameters.

6.2.1.1 Bending angle calculation:

GPS-LEO occultation geometry defining the atmospheric bending angle (α), the impact parameter (a), and the radius of the ray tangent point (r) is shown in Figure 1. The impact parameter (a) is defined, assuming spherical symmetry, as the perpendicular distance between the center of the Earth (more precisely the center of local curvature at the perigee of the occultation ray) and the ray asymptote at the GPS or LEO satellite. The atmospheric Doppler shift, Δf, can be related to the direction of the transmitted and received signals by the expression

$$\frac{d\gamma}{dt} = \lambda\Delta f = [v_t.\hat{k}_t - v_r.\hat{k}_r - (v_t - v_r).\hat{k}] \tag{1}$$

v_t and v_r – the transmitter (GPS) and receiver's (LEO) velocity respectively.

k_t and k_r – unit vectors in the direction of transmitted and received signal, respectively.

$\hat{k}$ - Unit vector in the direction from the transmitter to the receiver.

Equation (1) is difference of Doppler shift observed in the presence of the atmosphere and the Doppler shift that would be observed for the same transmitter-receiver geometry in the absence of the atmosphere. The first order relativistic contributions to the Doppler are identical in the two situations and cancel out. Equation (1) holds for atmosphere of any shape. However, (1) also has infinite number of solutions, since k_t and k_r are unknown, corresponding to four independent parameters. Therefore, certain assumptions have to be made on the shape of the atmosphere in order to derive the atmospheric bending from equation (1). To a good approximation, the neutral atmosphere is spherically symmetric. In order to account for the ellipticity of the Earth, the center of symmetry is taken to correspond to the circle of occultation plane which best fits the geoid near the tangent point. With the spherical symmetry assumption, equation (1) reduces to two equations in two unknowns

$$\frac{d\gamma}{dt} = (v_t \cos(\phi_t - \delta_t) - v_r \cos(\phi_r - \delta_r)) - (v_t \cos\phi_t - v_r \cos\phi_r) \tag{2(a)}$$

$$a = r_t n_t \sin(\theta_t + \delta_t) = r_r n_r \sin(\theta_r + \delta_r) \tag{2(b)}$$

Equation 2(b) is Bouger's law (equivalent to Snell's law in a spherically symmetric medium).

$\mathbf{r}_r$ and $\mathbf{r}_t$ are the vectors from the center of curvature to transmitter and receiver, respectively; $r_r = |\mathbf{r}_r|$, $r_t = |\mathbf{r}_t|$ and n_r and n_t are indices of refraction at the transmitter and receiver, respectively.
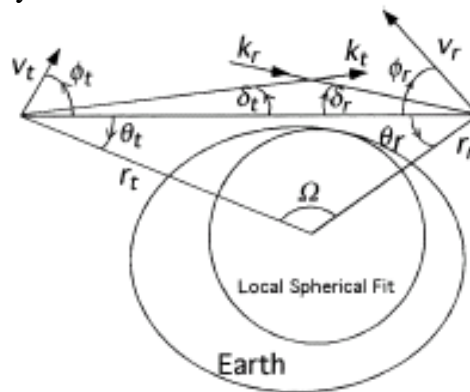

Figure 2. Occultation geometry defining the angles used in equations 2(a, b).

At the heights of the transmitter (~ 20000 km) and receiver (low earth orbit), the indices of refraction are assumed to be equal to 1. This approximation can be shown to introduce a very small error in the estimated bending in the ionosphere and it cancels completely after doing ionospheric calibration to estimate neutral atmospheric bending. The angles δ_t and δ_r are determined by simultaneously solving equations 2(a) and 2(b) (easily accomplished using Newton's method and a first guess of $\delta_t=0$ and $\delta_r=0$). The total bending angle is $\alpha=\delta_t+\delta_r$ and the corresponding impact parameter 'a' is obtained by equation 2(b).

If $\alpha_1(a_1)$ and $\alpha_2(a_2)$ be the bending angle as a function of the asymptotic miss distance for the L1 and L2 signals, respectively, then the linear combination

$$\alpha_{neut}(a_0) = \frac{f_1^2}{(f_1^2 - f_2^2)}\alpha_1(a_0) - \frac{f_2^2}{(f_1^2 - f_2^2)}\alpha_2(a_0) \qquad (3),$$

where α_1 and α_2 are interpolated to the same value of a_0, removes first-order ionospheric bending (which is proportional to f^{-2}). The calibration should not continue above a certain height, when the neutral atmosphere signature on the occulted signal is comparable to residual ionospheric effects or the receiver's thermal noise.

Deeper in the atmosphere, due to defocusing effects and the weakening of the signal, the L2 signal is not used when the signal to noise ratio drops below a certain limit. In that case, an extrapolation of the ionosphere correction is used from higher altitudes to correct for the ionosphere (Hocke 1997, Hocke *et al.,* 1997).

6.2.1.2 Retrieval of refractive index profile:

Inverse Abel transform technique is used to retrieve refractive index profile from bending angle profile (Hajj *et al.*, 1995; Kursinski *et al.*, 1996; Hocke 1997). Bending angle $\alpha_i(a_i)$ and the refractive index n at the perigee location of the ray is given by the forward Abel transform (e.g. Fjeldbo *et al.,* 1971):

$$\frac{\alpha_i}{2a_i} = \int_{x=a_i}^{\infty} \frac{d(\ln n)}{dx}\frac{dx}{\sqrt{(x^2 - a_i^2)}} \qquad (4)$$

Using inverse Abel transform, refractive index (n) is given as:

$$\ln(n(a)) = \frac{1}{\pi}\int_a^{\infty} \frac{\alpha(x)}{\sqrt{x^2 - a^2}}dx \qquad (5)$$

The upper limit of integral equation (5) requires knowledge of bending angle as a function of impact parameter up to the top of the atmosphere. In practice however, the estimated bending is reasonably accurate only up to a certain upper height, a_u. The refractivity profile is calculated by upward scaling of refractive index profile as:

$$N(a) = (n(a) - 1) \times 10^6 \qquad (6)$$

The refractivity, derived as a function of impact parameter, is redefined on a mean sea level altitude relative to the Earth's geoid so as to relate it to the geophysical parameters of temperature, pressure and water vapor partial pressure in the geoid frame.

6.3 Algorithm Functional Specifications

6.3.1 Retrieval of temperature (T), pressure (P) and water vapor partial pressure (e) from refractivity: Theoretical background

The refractivity, N, is related to temperature (T), pressure (P) and water vapor partial pressure (e) via (Gorbunov et al., 1996; Ware et al., 1996; Rocken et al., 1997; Kursinski et al., 1997; Steiner et al., 1999)

$$N = a1\frac{P}{T} + a2\frac{e}{T^2} - 40.3 \times 10^6 \frac{n_e}{f^2} + O(\frac{1}{f^3}) + a_w W_w + a_i W_i$$

(7)

with $a1$=77.6 K/mbar; $a2$=3.73x10^5 K^2/mbar; P – the total pressure; T – temperature; e – water vapor partial pressure; n_e – electron number density (m^{-3}); f – operating frequency (Hz); W_w and W_i being liquid water and ice content respectively in grams per cubic meter, a_w and a_i are 1.4 and 0.6 (cubic meter/grams) respectively. The first (second) term in equation (7) is usually known as hydrostatic (or, dry) term (wet term).

For realistic suspensions of water and ice, the last two terms of (7) are small in comparison with other terms and are neglected for practical purposes (Hajj et al. 2002). When the signal is passing through the ionosphere the first two terms of (7) can be ignored, as well as higher order ionospheric terms. Therefore, measurement of n directly corresponds to electron density in the ionosphere.

In the neutral atmosphere (tangent point height < 60 km), the ionospheric calibration process effectively removes the first order ionosphere term (1/f^2) in (7). In order to solve for P, T and/or e, given N, one has to use additional constraints of hydrostatic equilibrium and the ideal gas law:

$$\frac{dP}{dh} = -g\rho$$

(8)

$$\rho = \rho_d + \rho_w = \frac{m_d P}{TR} + \frac{(m_w - m_d)e}{TR}$$

(9)

Where, h is height; g is the acceleration due to gravity; ρ, ρ_d, ρ_w total, dry air and water vapor densities respectively; m_d, m_w the mean molecular mass of dry air (28.97 g/mole) and water vapor (18.0 g/mole), respectively; R is the universal gas constant.

Combining (8) and (9) and, using (7) (ignoring ionospheric, ice and liquid water terms) to substitute for P/T, we obtain

$$\frac{dP}{dh} = -\frac{gm_d}{a1R}N + \frac{a2gm_d}{a1R}\frac{e}{T^2} + \frac{g(m_d - m_w)}{R}\frac{e}{T}$$

(10)

Given N, we have a system of two equations ((7) and (10)) and three unknowns (T, P, and e). Since saturation vapor pressure decreases rapidly with decreasing temperature, e can be ignored above the tropospheric height corresponding to 230 K; therefore given N, both T and P can be solved for in the upper troposphere and stratosphere from (7) and (10) and a boundary condition (usually taken to be a temperature boundary condition at ~60 km estimated from a climatology or an atmospheric model). What we get are the "dry" temperature and pressure, accurate to real temperature and pressure in the water vapor scarce

region obtained in the upper troposphere and beyond. The "dry" T has a cold bias in the lower troposphere below 230K as shown in figure 3.
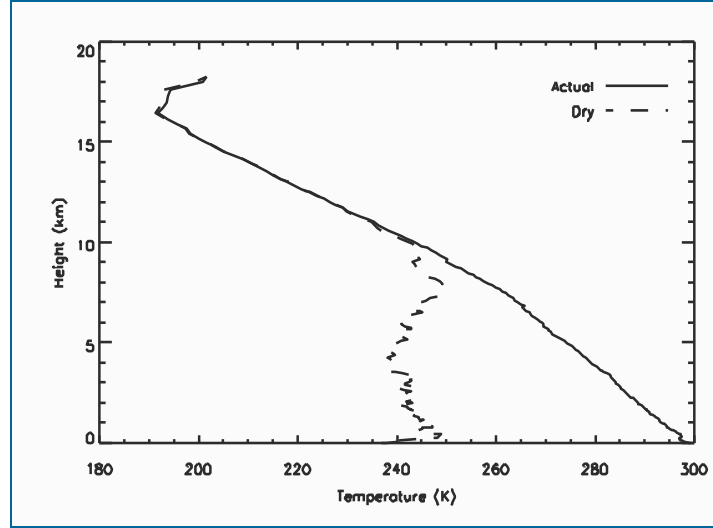

Figure 3. A depiction of cold bias in "dry" temperature below 10km

Realistic temperature and pressure profile require inclusion of water vapor pressure (e) term in equation (7) and (10) for retrieval below 230K. This demarcation at

230K temperature is defined as the water vapor point (O' Sullivan et al. 2000). The water vapor point is observed to vary in different latitude zones. For the tropics (30S-30N), the water vapor point at 230K is determined through a sensitivity study of the error statistics of retrieved T, P and e from refractivity, N to different choices of water vapor point (Shyam et al., 2009). In altitude terms, the water vapor point for the tropics range from 10-12km. Below this altitude, water vapor has a non-negligible concentration and contributes significantly to refractivity. Thus, the algorithm goes for a composite retrieval (to be called "Wet retrieval") of all the three unknowns simultaneously.

"Wet" Retrieval

The algorithm approximates temperature, for the region below the "water vapor point (wvp)", to be a quadratic function of the natural logarithm of atmospheric pressure. Between the estimated water vapor point and the surface (or, the lowest altitude at which a' priori *P* and *T* are available), temperature is assumed to vary as a quadratic function of natural logarithm of *P* (denoted by σ) i.e. *T* (σ) = *a* + *b**σ + c*σ². We have T and σ at water vapor point, where the dry temperature and pressure are approximated as actual temperature and pressure and the surface (known from meteorological observations or reanalysis of Numerical weather prediction models like ECMWF or NCEP), giving two equations for the temperature quadratic i.e.,

$$T(\sigma_s) = a + b\sigma_s + c\sigma_s^2 \tag{11}$$

Where σ_s is the natural logarithm of surface pressure.

$$T(\sigma_{wv}) = a + b\sigma_{wv} + c\sigma_{wv}^2 \tag{12}$$

Where σ_{wv} is the natural logarithm of pressure at the water vapor point.

A third equation is written using hydrostatic approximation as given under

$$\int_{\sigma_0}^{\sigma_w} T(\sigma)d\sigma = -\int_{z_0}^{z_w} \frac{g}{R_{air}}dz \tag{13}$$

The right hand side of (13) is evaluated by approximating the gas constant for air (R_{air}), as that of dry air (R_{dry}), as we do not have any knowledge of water vapor in the beginning. Solving equations (11) to (13), one obtains the three coefficients for the temperature quadratic. Once a first estimate of temperature quadratic is made, temperature profile in the first iteration is evaluated using dry pressure and water vapor pressure is calculated using the equation

$$e = \frac{T^2 N - 77.6 PT}{3.73 \times 10^5} \tag{14}$$

Once a first estimate of **e** is made water vapor mixing ratio (w) is calculated using the formula

$$w = 0.622 \times \frac{e}{P} \tag{15}$$

Thereafter, the virtual temperature (T_v) profile is calculated using the formula

$$T_v = \frac{T(1.0 + (1.61 * w))}{(1.0 + w)} \tag{16}$$

Once a virtual temperature profile is estimated, the pressure profile is re-estimated using the hydrostatic equation

$$P = P_w \exp(-\int_{z_w}^{z} \frac{g}{R_{dry}T}dz) \tag{17}$$

Where, P_w is pressure at the water vapor point z_w.

Re-estimated pressure is then used to calculate temperature, water vapor (and virtual temperature) profiles in successive iterations until the three profiles converge. It is worth noting that two options are possible here (not pointed out by O'Sullivan et al. (2000)): (i) keep the coefficients of temperature quadratic same throughout the iterations with $R=R_{dry}$ approximation in equation (13), and (ii) update the right hand side integral in equation (13) with water vapor information and hence solve for fresh temperature quadratic coefficients in each iteration which requires refractivity profile available up to the surface or lower altitude. Currently, only the first option is considered as the radio occultation derived refractivity profiles do not reach the surface and are often available only up to altitudes of 1 km and above only. Also, knowledge of near-surface refractivity requires information on surface specific humidity and hence in practice the second option is not feasible.

6.4 Operational Implementation

For ease of operational implementation, the algorithm will be formalized into a software to be designed and developed in a modular fashion. Different functions of the algorithm, as compositely shown in the flowchart in the following sub-section, will be divided into five sub-modules, the first four sub-modules performing specific pre-processing of the principal input (i.e. Level-1 refractivity profile) as well as the auxiliary data, dry computation and water vapor point

location before feeding into the fifth module for "wet retrieval". The next sub-section depicts a detailed flowchart of the algorithm

6..4.1 Algorithm Flowchart
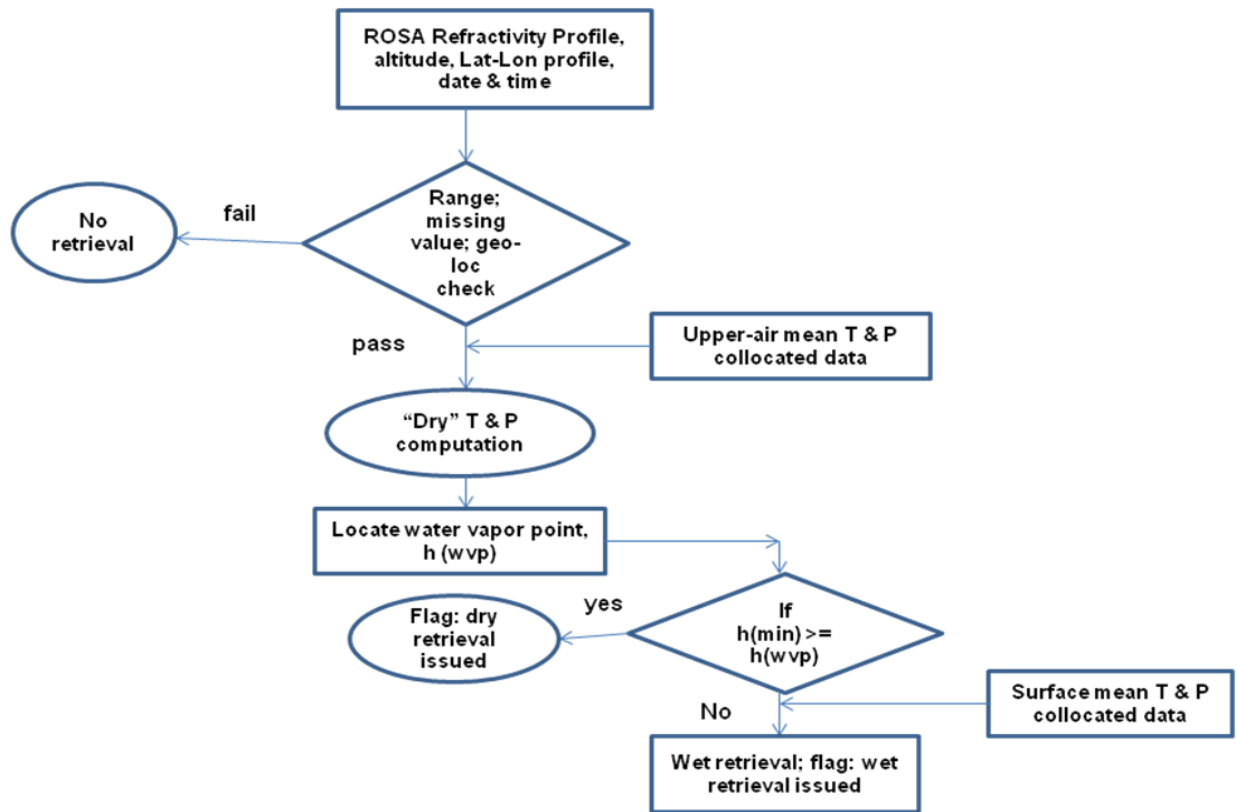
6.4.2 Inputs:

The inputs for the algorithm can be classified as static and dynamic as detailed in the next sub-sections:

6.4.2.1 Static Data

Parameter	Resolution	Accuracy	Source
Meteorological constants	N.A.	Upto 3 decimal place	Hajj et al. 2002
Coefficients of Forward model	N.A.	Upto 3 decimal place	-Do-

6.4.2.2 Dynamic Data

Parameter	Resolution	Accuracy	Source
Neutral atmospheric Refractivity profile from ROSA;	0.1 – 1.5 km (vertical); 200-300 km (Horizontal)	~ 3-5% (below 5km); ~1-2% (above 5km)	ROSA operational chain front-end

Spatial (Latitude & Longitude profile); Temporal (Time) data	0.1 – 1.5 km (vertical); scalar	N.A	ROSA operational chain front-end
zonal mean temperature & pressure	5km (vertical) ; 10deg (horizontal)	5-10K (20-50km);	CIRA-86 (Fleming et al., 1990)
Surface mean monthly temperature & pressure	1°×1°	Up to 1K ; 0.05-2hPa	Generated in-house using NCEP analyses
Surface altitude	1°×1°	Less than 1m	Generated using NCEP data

6.4.3 Outputs

Parameter	Unit	Min	Max	Accuracy *	Resolution
Temperature	K	123.15	373.15	3-5 K (below 5km); 1-2 K (5-20 km); 1.5-3 K (> 20km)	~ 300 km horizontal and 0.2 – 1.5 km in the vertical
Pressure	hPa	~0.0	1200.0	2 – 10 hPa	Same as above
Water Vapor Partial Pressure	hPa	0.0	60.0	0.5 to 1 hPa	Same as above and limited to altitudes below ~10 km
First-Cut Parameters (from "Dry Retrieval")					
Dry Temperature	K	123.15	300.0	Same as Temperature (> 15 km);	Same as above

Dry Pressure	hPa	~0.0	1200.0	5-15hPa	Same as above

∗ **Depends on the expected refractivity accuracy** (Ao et al., 2003)

6.4.4 Format of the Output:

Following are the output parameters to be generated by this operational algorithm in the output file: Latitude, longitude, height, refractivity, temperature, pressure and water vapor partial pressure, dry temperature and dry pressure. In addition to the profile of output parameters, time and location are mentioned in the file as scalars. The overall format of the output file is in standard netcdf.

6.5 Validation:

6.5.1 Data Required:

i) Comparison with collocated radiosonde measurements of temperature, pressure and water vapor pressure profile.
ii) Comparison with collocated NCEP/ECMWF or both.
iii) Comparison with existing COSMIC data, collocated in space and time.

6.5.2 Methods of Validation:

The validation is to be carried out between the various "truth" data, as mentioned above, and ROSA retrieved geophysical parameters, collocated spatially and temporally as per the following collocation criteria.

Collocation criteria for each parameter:

Temporal (hr) / Spatial	1 ˚	2 ˚	3˚
0.5	water vapor profiles	water vapor profiles	Temperature & water vapor profiles
1	water vapor profiles	water vapor profiles	--------DO--------
2	water vapor profiles	water vapor profiles	------ DO-------

The validation results will be expressed in terms of arithmetic mean and standard deviation of the difference of parameter at each level using the formulae:

Mean deviation at each pressure/height level,

$$\overline{\Delta X(l)} = \frac{1}{M(l)} \sum_{i=1}^{M(l)} \left(X_{Test}(i,l) - X_{True}(i,l) \right)$$

And its standard deviation at each pressure/height level,

$$\sigma_{\Delta X}(l) = \sqrt{\frac{1}{M(l)-1} \sum_{i=1}^{M(l)} (X_{Test}(i,l) - X_{True}(i,l))^2}$$

Where, l is the pressure level, i the collocation pair index and $M(l)$ is the number of collocation pairs at level l

6.6 Technical Issues:

➢ Radio occultation measurements are over a location of the earth depending on the position of GPS and LEO satellites. The exact location over which radio occultation measurements are possible, require prior knowledge of GPS and Megha-Tropiques orbit. One may expect 500 to 800 occultations per day spread in the domain (30S-30N; 180W-180E) with dense occurrence around 10-20S/N.

➢ Theoretically, the GPS-RO data of reliable quality may range from 0 – 60km in the neutral atmosphere. Practically, the measurements are reliable between altitudes of 5 to 30 km height, irrespective of the atmospheric dynamics. Since, ROSA coverage will be confined to the tropics where moisture gradients creates multipath conditions, advanced techniques to retrieve refractivity profile by an open-loop processing as implemented in global missions like COSMIC, GRAS etc., may be required to penetrate to near surface altitudes ~ 0.1 km or less. Examination of COSMIC profiles over the ocean indicates that more than 90% of the radio occultation refractivity measurements are available up to an altitude of 0.5 km from the mean sea level.

➢ The algorithm uses the CIRA-86 COSPAR upper-air atmospheric model data of zonal mean temperature and pressure available up to 120km for the computation of hydrostatic integral. The accuracy of the upper-air data as quoted by COSPAR has been assumed suo motu, in the absence of ways to validate them.

➢ The monthly mean surface temperature, pressure and altitude data are generated from NCEP analyses at global grid of 1deg x1 deg resolution as first guess estimates. The standard deviations (all months and for 30S-30N) of mean surface temperature and mean surface pressure are ~ 1K and 0.05-2.0hPa respectively. To get a more accurate first guess, the use of daily forecast of NCEP, nearest to ROSA occultation event time and location is imperative.

6.7 References:

1. Ao, C.O., T. K. Meehan, G.A. Hajj, A.J. Mannucci, and G. Beyerle, 2003. Lower-troposphere refractivity bias in GPS occultation retrievals. J. Geophys. Res., 48, 4577, doi:10.1029/2002JD003216.

2. Beyerle, G., M.E. Gorbunov, and C.O. Ao, 2003. Simulation studies of GPS radio occultation measurements. Radio Sci., 38, 1084, doi:10.1029/2002RS002800.

3. Fjeldbo G., A. J. Kliore, and Von R. Eshleman, 1971. The neutral atmosphere of Venus as studied with the Mariner V Radio Occultation Experiments. *The Astronomical Journal,* 76, 123-140.

4. Fleming, E.L., S. Chandra, J.J. Barnett, and M. Corney, 1990. Zonal mean temperature, pressure, zonal wind and geopotential heights as functions of latitude. COSPAR International Reference Atmosphere: 1986, Part-II, Middle atmosphere models. Advance Apace Res. 10, No. 12, 11-59, 1990.

5. Gorbunov M. E., A. S. Gurvich, and L. Bengtsson, 1996. Advanced algorithm of inversion of GPS/MET satellite data and their application to reconstruction of temperature and humidity, *Rep. 211,* Max-Planck-Institut fur Meteorologie, Hamburg, Germany.

6. Hajj G.A., E. R. Kursinski, W. I. Bertiger, S. S. Leroy, T. K. Meehan, L. J. Romans, and J. T. Schofield, 1995. Initial results of GPS-LEO occultation measurements of Earth's atmosphere obtained with the GPS-MET experiment. *Paper presented at the IUGG XX1 General Assembly,* Int. Union of Geod. And Geophys., Boulder, CO, Jul.2-14, 1995.

7. Hocke K, 1997. Inversion of GPS meteorology data, *Ann. Geophysicae,* 15, 443-450.

8. Hocke K., G. Kirchengast and A. K. Steiner, 1997. Ionospheric correction and inversion of GNSS occultation data: problems and solutions, *IMG/UoG Tech. Rep. For ESA/ESTEC No.2/97,* Inst. of Meteorol. and Geophys., Univ. of Graz, Austria., 35 pp.

9. Kirchengast, G., J. Hafner, and W. Poetzi, 1999. The CIRA-86aQ_UoG model: An extension of the CIRA-86 monthly tables including humidity tables and a Fortran 95 global moist air climatology model. Eur. Space Agency, IMG/UoG Techn. Rep. 8.

10. Kursinski E. R., G. A. Hajj, W. I. Bertiger, S. S. Leroy, T. K. Meehan, L. J. Romans, J. T. Schofield, D. J. McCleese, W. G. Melbourne, C. L. Thrnton, T. P. Yunck, J. R. Eyre, and N. Nagatani, 1996. Initial results of radio occultation observations of Earth's atmosphere using the global positioning system, *Science,* 271, 1107-1110.

11. Kursinski E. R., G. A. Hajj, K. R. Hardy, J. T. Schofield, and R. Linfield, 1997. Observing Earth's atmosphere with radio occultation measurements using the Global Positioning System, *J. Geophys. Res.,* 102, 23429-23465.

12. O'Sullivan, D. B., B. M. Herman, D. Feng, D. E. Flittner, and D. M. Ward, 2000: Retrieval of water vapor profiles from GPS/MET radio occultations. *Bull. Amer. Meteor. Soc.,* 81, 1031-1040.

13. Rocken, C., R. Anthes, M. Exner, D. Hunt, S. Sokolovsky, R. Ware, M. Gorbunov, W. Schreiner, D. Feng, B. Herman, Y. H. Kuo, and X. Zou, 1997. Analysis and validation of GPS/MET data in the neutral atmosphere, *J. Geophys. Res.,* 102, 29849-29866.

14. Steiner A. K., G. Kirchengast, and H. P. Ladreiter, 1999. Inversion, error analysis, and validation of GPS/MET occultation data, *Ann. Geophysicae.,* 17, 122-138.

15. 15. Shyam A., D. Jagadeesha and P C Joshi, 2009. Sensitivity studies in retrieval of geophysical parameters from radio occultation derived refractivity, IITP-18 Report, Space Applications Centre (ISRO), Ahmedabad.

16. Ware R., M. Exner, D. Feng, M. Gorbunov, K. Hardy, B. Herman, Y. Kuo, T. Meehan, W. Melbourne, C. Rocken, W. Schreiner, S. Sokolovsky, F. Solheim, X. Zou, R. Anthes, S. Businger, and K. Trenberth, 1996. GPS sounding of the atmosphere from Low Earth Orbit: preliminary results, *Bull. Am. Meteorol. Soc.,* 77.